Macalester Journal of Physics and Astronomy

Volume 11
Issue 1 *Spring 2023*

Article 3

June 2023

Extension of the LUX-ZEPLIN NR Background to 600 phd

Jackson Codd
Macalester College, jcodd1@macalester.edu

Follow this and additional works at: https://digitalcommons.macalester.edu/mjpa

Part of the Elementary Particles and Fields and String Theory Commons

Recommended Citation

Codd, Jackson (2023) "Extension of the LUX-ZEPLIN NR Background to 600 phd," *Macalester Journal of Physics and Astronomy*: Vol. 11: Iss. 1, Article 3.
Available at: https://digitalcommons.macalester.edu/mjpa/vol11/iss1/3

This Honors Project - Open Access is brought to you for free and open access by the Physics and Astronomy Department at DigitalCommons@Macalester College. It has been accepted for inclusion in Macalester Journal of Physics and Astronomy by an authorized editor of DigitalCommons@Macalester College. For more information, please contact scholarpub@macalester.edu.

Macalester College

Extension of the LUX-ZEPLIN NR Background to 600 phd

Abstract

In June 2022, the LUX-ZEPLIN collaboration released its first results, with the most precise measurements of any direct dark matter detector. The findings were calculated using the expected spin-independent WIMP-nucleon interaction model, which would result in small energies deposited in the detector. Therefore, the background of non-dark interactions was calculated for events with S1 areas up to 80 phd (Aalbers et al. 2022). In order to increase the sensitivity to high energy WIMP-nucleon interaction events, as predicted by other models, we extended the non-dark NR background to events with S1 areas of up to 600 phd. We found a large contribution to the NR background from ER leakage. Though the leakage peaked below 80 phd, the leakage rate at 80 phd is roughly 1% for all interaction models, and falls to zero between 150 phd and 200 phd. The expected number of xenon-based MSSI is roughly 0.015 for all spin-dependent interaction models, peaking at high S1 areas. We found the rate of cathode-based MSSI to be zero. The wall based MSSI rate we calculated is significantly higher than is shown by the data, which likely means that the model of the electric field in the detector is incorrect.

Keywords

Dark Matter, Direct Detection

This honors project - open access is available in Macalester Journal of Physics and Astronomy:
https://digitalcommons.macalester.edu/mjpa/vol11/iss1/3

MACALESTER COLLEGE

Extension of the LUX-ZEPLIN NR Background to 600 phd

by

Jackson Codd

in the

Department of Physics and Astronomy

Advisors: Dr. John Cannon, Dr. Bjoern Penning

April 2023

Declaration of Authorship

I, Jackson Codd, declare that this thesis titled, 'Extension of the LUX-ZEPLIN NR Background to 600 phd' and the work presented in it are my own. I confirm that:

- This work was done wholly or mainly while in candidature for a research degree at this University.
- Where any part of this thesis has previously been submitted for a degree or any other qualification at this University or any other institution, this has been clearly stated.
- Where I have consulted the published work of others, this is always clearly attributed.
- Where I have quoted from the work of others, the source is always given. With the exception of such quotations, this thesis is entirely my own work.
- I have acknowledged all main sources of help.
- Where the thesis is based on work done by myself jointly with others, I have made clear exactly what was done by others and what I have contributed myself.

Signed: Jackson Codd

Date: 05/01/2023

MACALESTER COLLEGE

Abstract

Department of Physics and Astronomy

by Jackson Codd

In June 2022, the LUX-ZEPLIN collaboration released its first results, with the most precise measurements of any direct dark matter detector. The findings were calculated using the expected spin-independent WIMP-nucleon interaction model, which would result in small energies deposited in the detector. Therefore, the background of non-dark interactions was calculated for events with S1 areas up to 80 phd (Aalbers et al. 2022). In order to increase the sensitivity to high energy WIMP-nucleon interaction events, as predicted by other models, we extended the non-dark NR background to events with S1 areas of up to 600 phd. We found a large contribution to the NR background from ER leakage. Though the leakage peaked below 80 phd, the leakage rate at 80 phd is roughly 1% for all interaction models, and falls to zero between 150 phd and 200 phd. The expected number of xenon-based MSSI is roughly 0.015 for all spin-dependent interaction models, peaking at high S1 areas. We found the rate of cathode-based MSSI to be zero. The wall based MSSI rate we calculated is significantly higher than is shown by the data, which likely means that the model of the electric field in the detector is incorrect.

Acknowledgements

I would like to thank Dr. Greg Rischbieter for helping immensely with this project. From patiently explaining the inner workings of the LZ detector and particle physics to identifying methods of background calculation that I would never have thought of, Greg's help was invaluable. The insights he provided allowed me to understand the importance of the work that I was doing, motivating me to go forward, and my project would be nowhere near what it is today without his help.

Dr. Bjoern Penning for bringing me into his team and providing support through my entire project. Though I had almost no experience with dark matter, he encouraged me to learn and work independently early on. The feedback he gave on the thesis cleared up questions I still had on the interaction mechanisms and provoked me to present the data in new ways.

Dr. John Cannon for the excellent reviews of my early thesis. His comments elucidated areas lacking in full explanation and many other ways to improve readability. He was always happy to meet and discuss the project to keep me on track, even when not on campus. Additionally, over the past few years he has imparted his enthusiasm for physics, driving my passion to go above and beyond... the stars.

Dr. James Heyman for the excellent academic advice he provided over the years. He supported my goals and encouraged me to apply for summer research. He also let me know when I was overloading myself, and how to prevent from burning out, which I greatly appreciate.

Michael Williams for lending his expertise in event reconstruction as well as his great attitude.

My parents for always showing (hopefully) genuine enthusiasm for my work as well as forcing me to improve my fundamental understanding and communication skills when I tried to explain whatever nonsense I was working on to them.

The entire Physics and Astronomy department for the support and encouragement they have provided over the past 4 years.

Contents

Declaration of Authorship i

Abstract ii

Acknowledgements iii

List of Figures vi

List of Tables xi

1 Introduction 1
- 1.1 The LUX-ZEPLIN Detector . . . 2
- 1.2 Data Collection . . . 6
- 1.3 The NR Background . . . 8
  - 1.3.1 MSSI Events . . . 9
  - 1.3.2 ER Leakage . . . 12

2 Computational Methods 13
- 2.1 WIMP-Nucleon Interaction Operators . . . 13
- 2.2 Near Miss MSSI Analysis . . . 14
  - 2.2.1 Data Cuts . . . 16
  - 2.2.2 Hand Scanning . . . 21
- 2.3 MSSI and ER Leakage Rate . . . 22
  - 2.3.1 WIMP-nucleon Recoil Bands . . . 22
  - 2.3.2 ER Leakage Calculations . . . 24
  - 2.3.3 MSSI Leakage Calculations . . . 24

3 Results and Analysis 25
- 3.1 Near Miss MSSI Search . . . 25
- 3.2 Pileup Events . . . 27
- 3.3 MSSI Leakage Rate . . . 30
- 3.4 ER Leakage Rate . . . 31

4 Conclusion 36

A Fiducial Volume Cut Analysis **38**

B WIMP-Nucleon Recoil Bands **42**

Bibliography **46**

List of Figures

1.1 The 90% confidence limit of the mass-cross section function for spin-independent WIMPs is shown by the black line. The 1σ and 1σ sensitivity projections are shown in green and yellow, with the median sensitivity projection shown by the dotted black line. Sensitivities for previous direct detection studies are shown and labeled (Aalbers et al. 2022) 3
1.2 Model of the LUX-ZEPLIN Detector, with large components labeled and a human for scale (Mount et al. 2017) 4
1.3 Diagram of the Time-Projection Chamber collecting data from a particle interaction. In the diagram, a particle enters the detector and deposits some of its energy on a xenon atom, which then emits electrons and photons. Taken from Mount et al. (2017) 5
1.4 Comparison of the shape and size of S1 and S2 signals. The S1 signal, seen on the left, is significantly weaker and lasts for less than half a nanosecond. The signal strength quickly peaks before slowly decaying back to zero. The S2 signal on the right is a much stronger signal and lasts 4 ns. The amplitude follows a roughly Gaussian distribution over time. 6
1.5 Plot of the median and 90%-10% probability distribution of the ER and NR bands based on simulation data. S1c and S2c represent the corrected area of the S1 and S2 signal detections, measured in photons detected by the PMTs. The S2 signal is plotted on a log scale, meaning that the S2 strength is several orders of magnitude greater for ER events at all but the lowest energies, leading to easy discrimination. 7
1.6 Plot of event detections from the first 60 days of run time. 12 events are measured within the NR band, between the dotted red lines, with most of the remainder falling towards the middle of the ER band. Some or all of the events in the NR band are likely the result of ER interactions (Aalbers et al. 2022). 8
1.7 Diagram of the electric field strength relative to location in the detector, with radius from the center plotted on the x-axis. Potential contours are shown in black. The electric field is significantly stronger and points the opposite direction below the cathode, with this region being designated the Reverse Field Region (Mount et al. 2017). 10

1.8 Model of the electric field strength relative to the drift region near the wall of the detector, with radius from the center plotted on the x-axis and height on the y-axis. This region is significantly enlarged to show the small fluctuations clearly. Electric field lines are shown in white, with dead zones in dark blue (Plot created by Reed Watson). 11

2.1 Quantum Mechanical Operators for WIMP-nucleon interactions. Operators 2 and 16 are linear combinations of other operators and thus are not shown (Baum et al. 2018). 14

2.2 Distribution of S1 and combined S2 area of all events included in this study. ER and NR bands are overlaid in blue and red, respectively. As the events are double scatters, their reconstructed S1 and S2 areas are each roughly double what they would be for single scatters, causing an offset from the ER and NR bands. Most events fall near the ER and NR bands, though there are many events outside these bands, particularly at lower energies. 15

2.3 Comparison of random noise incorrectly marked as S1 (top) to an expected S1 signal (bottom). Taken from a single scatter event using the LZ event viewer. Note that the amplitude scale for the noise based S1 has been magnified 10x. 16

2.4 Event density of double scatters compared to location in the detector. Horizontal position is shown as R^2 to remove bias as a result of larger radii containing a larger volume. 18

2.5 Plot of double scatters that have passed all standard data cuts. There seem to be false detections remaining at the low end the of S1 area axis, but most of the noise has been eliminated. 19

2.6 61 double scatters that passed all quality cuts. The xenon and diagonal cuts are shown in black and the ER band is shown in blue. There are two primary groupings of double scatters, one with lower energies and one with high energies. 20

2.7 The waveform of a pileup event that was incorrectly marked as a double scatter. Due to the small size of the first S1 signal, it was not properly identified. 21

2.8 Ratio of events with 300 phd S1 detection to 50 phd S1 detection. Ratio rises for higher mass WIMPs, and is consistently highest for operator 06, followed by operators 15, 13, 10, and 03. 23

3.1 Near Miss MSSI events displayed with ER band shown in blue. Note that the events are more concentrated at higher energies, with none below 200phd. 25

3.2 Near Miss MSSI plotted by their location in the TPC. Drift time is roughly proportional to vertical depth and is plotted in reverse so that events near the top of the detector are shown at the top of the plot. There are many events near the outer walls but virtually none near the cathode. 26
3.3 Pileup event position using corrected drift time. All drift times fall between 950 μs and 952 μs. This is the depth of the cathode and falls outside the fiducial volume. 28
3.4 Overlaid histograms comparing the reconstructed event energy for pileup events and real events. Apart from a single outlier, the pileup events have significantly lower energy and a narrower energy distribution. 29
3.5 The waveform of a characteristic pileup event. The S1 at the far left was small enough that this event was mis-classified as a double scatter. The drift time for each scatter is shown with the red arrow marking the time between the S1 and S2 detections. 30
3.6 Histogram of the time separation between pileup events. If these were caused by two radioactive decays, we would expect the time separation to follow $A = A_0 e^{-\lambda t}$. 31
3.7 ER band leakage rate as a function of S1 area. Plotted are the leakages below the band median and 90% confidence level for the default flat NR band (Operator 01) as well as positive and negative uncertainties in the band. 32
3.8 ER band leakage rate as a function of S1 area. Plotted are the leakages below the band median and 90% confidence level for Operator 03 with WIMP masses of 400GeV and 4000GeV. The leakage below the default flat band is displayed for comparison. 33
3.9 ER band leakage rate as a function of S1 area. Plotted are the leakages below the band median and 90% confidence level for Operator 06 with WIMP mass of 400GeV. The leakage below the default flat band is displayed for comparison. 33
3.10 ER band leakage rate as a function of S1 area. Plotted are the leakages below the band median and 90% confidence level for Operator 10 with WIMP masses of 400GeV and 4000GeV. The leakage below the default flat band is displayed for comparison. 34
3.11 ER band leakage rate as a function of S1 area. Plotted are the leakages below the band median and 90% confidence level for Operator 13 with WIMP masses of 400GeV and 4000GeV. The leakage below the default flat band is displayed for comparison. 35

A.1 Plot of double scatters that have passed all standard data cuts, including FV cut 1. This series of cuts has eliminated much of the random noise in addition to significant amounts of low energy ER events which we would like to study. 39

A.2 Plot of the positions of double scatters that have passed all standard data cuts, including FV cut 1. There are no events outside the FV, though such events are similar to MSSI. 39
A.3 Plot of double scatters that have passed all standard data cuts, including FV cut 2. This series of cuts has eliminated much of the random noise but leaves many of the low energy ER events which we would like to study. 40
A.4 Plot of the positions of double scatters that have passed all standard data cuts, including FV cut 2. There are some events outside the FV, though many are excluded. 40
A.5 Plot of double scatters that have passed all standard data cuts, including FV cut 3. This data is still very noisy, as events significantly above the ER band or below the NR band are unlikely to be real. . 41
A.6 Plot of the positions of double scatters that have passed all standard data cuts, including FV cut 3. There are many events outside the FV, including those that may not have a real scatter in the FV. . . 41

B.1 The flat NR band expected for spin independent WIMP-nucleon interactions plotted against simulated MSSI and ER events. The events that fall within the NR band form the NR background. The fringes for the positive uncertainty in the flat NR band is shown above the top dotted line and the negative uncertainty is shown below the bottom line. 42
B.2 The NR band expected for nucleon interactions by 400GeV mass WIMPS through operator 03, plotted against simulated MSSI and ER events. The events that fall within the NR band form the NR background. 42
B.3 The NR band expected for nucleon interactions by 4000GeV mass WIMPS through operator 03, plotted against simulated MSSI and ER events. The events that fall within the NR band form the NR background. 43
B.4 The NR band expected for nucleon interactions by 400GeV mass WIMPS through operator 06, plotted against simulated MSSI and ER events. The events that fall within the NR band form the NR background. 43
B.5 The NR band expected for nucleon interactions by 400GeV mass WIMPS through operator 10, plotted against simulated MSSI and ER events. The events that fall within the NR band form the NR background. 44
B.6 The NR band expected for nucleon interactions by 4000GeV mass WIMPS through operator 10, plotted against simulated MSSI and ER events. The events that fall within the NR band form the NR background. 44

B.7 The NR band expected for nucleon interactions by 400GeV mass WIMPS through operator 13, plotted against simulated MSSI and ER events. The events that fall within the NR band form the NR background. 45
B.8 The NR band expected for nucleon interactions by 4000GeV mass WIMPS through operator 13, plotted against simulated MSSI and ER events. The events that fall within the NR band form the NR background. 45

List of Tables

2.1 Events removed in each step of the data selection process. Both the absolute number of events and the percentage of remaining events were removed is given. While the S1 and S2 quality cuts removed the most events, the Diagonal cut had by far the greatest efficiency. 22

3.1 Xenon-based MSSI leakage into NR band for a variety of interaction models. Leakage shown is expected number of events in the first observing run of LZ. The high uncertainty is primarily the result of the large estimated systematic uncertainties in the calculation for the total xenon-based MSSI. 32

CHAPTER 1: Introduction

The identification of the particles that constitute dark matter is one of the most challenging problems in modern physics. Since Fritz Zwicky first noticed the abundance of nonluminous mass in galaxy clusters using the virial theorem (Andernach & Zwicky 1933), dark matter has been the subject of countless studies using techniques from particle collision to gravitational lensing. While these studies have yet to detect any form of dark matter, they have resulted in invaluable insight into its characteristics. Though observation suggests that dark matter makes up roughy 85% of the total matter in the universe (Mullat 2016), it does not interact through the strong or electromagnetic forces, allowing light and other matter to pass through it without resistance. The only force that dark matter has been observed to interact with is gravity.

The current leading theory for dark matter composition is Cold Dark Matter (CDM). CDM theory predicts that dark matter is composed of Weakly Interacting Massive Particles, hereafter referred to as WIMPs, with estimated mass between 2 GeV and 100 TeV. WIMPs are nonbaryonic, meaning they are not made up of the atoms and molecules that constitute the matter we are used to (Roszkowski et al. 2018). This matter is referred to as "cold" because its relatively high mass particles causes it to be non-relativistic at the time of decoupling, the time at which photons began to travel freely, and thus the time from which we can observe light.

While dark matter does not interact via the electromagnetic, weak, or strong forces, the standard model predicts that it should interact with baryonic matter through weak coupling with standard model particles (Roszkowski et al. 2018) This theorized interaction forms the basis for all three primary methods to search for dark matter: indirect detection, particle collision, and direct detection.

Indirect DM detection uses observational astronomy to search for the remnants of WIMP decay in space. Telescopes such as the High Energy Antimatter Telescope peer into regions with high expected dark matter density, such as galactic centers. They look for the positrons and antiprotons, among other particles, that are predicted to be created as a result of dark matter annihilation. By comparing this

to the rate of these particles from non-dark sources, researchers can theoretically calculate the small-scale structure of dark matter (Bertone & Merritt 2005).

The particle collision method utilizes particle accelerators such as the Large Hadron Collider to search for dark matter. Using the extreme energies and precision provided by the detectors in such colliders, researchers measure the collision of particles travelling nearly the speed of light to instigate interactions with a high energy threshold. By observing the particles emitted by the interaction, the researchers identify the resulting energy and momentum of the system. As these values must be conserved, any difference in energy or momentum after the interaction must have been emitted in a particle the instruments are unable to detect, dark matter (Abe et al. 2020).

Finally, direct detection projects use highly specialized sensors to detect even the faintest energies that a DM particle may deposit in a detector through interactions with baryonic matter. These detectors use the observation that dark matter is dispersed roughly evenly through the galactic halo, and thus many WIMPs must be passing through the Earth every second. while the interaction rate with baryonic matter is low, it is not predicted to be zero. Thus, large containers of ultra-pure material are constructed to attempt to measure these interactions (Bertone & Merritt 2005). The work in this project is performed as part of the direct dark matter detection collaboration, LUX-ZEPLIN.

1.1 The LUX-ZEPLIN Detector

The LUX-ZEPLIN (LZ) collaboration is made up of hundreds of members at more than 35 institutions across the globe. LZ is one of three second generation direct detection dark matter experiments, and is primarily formed of researchers from the first generation LUX and ZEPLIN experiments (Mount et al. 2017). The second generation of detectors are several times larger than the first generation, and include more precise instruments, Therefore, they have the ability to identify WIMPs with much smaller cross sections than the first generation were able to.

In June of 2022, LZ released the results from its first observing run, taken from 60 days of run time out of a planned 1000 days. Although it used merely 6% of the total exposure time, the June publication significantly lowered the upper limit of the DM cross section function for all masses. At its most sensitive mass, LZ reduced the limit by a factor of 6.5 over past experiments, making it the most sensitive direct dark matter detector for the foreseeable future (Aalbers et al. 2022). The mass-cross section limit is compared to previous studies in Figure 1.1.

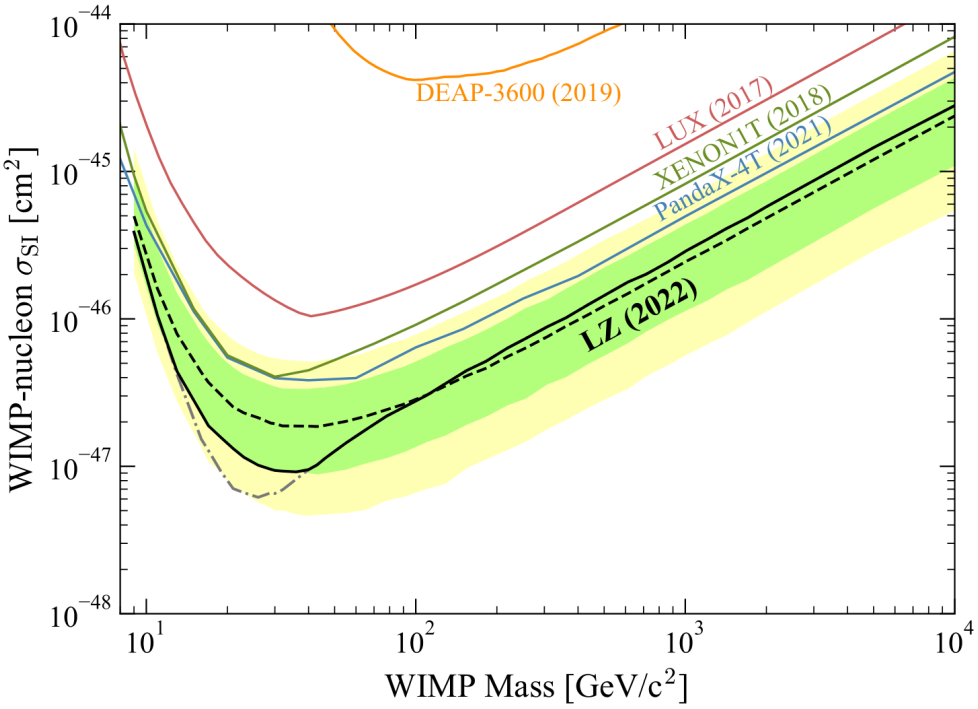

FIGURE 1.1: The 90% confidence limit of the mass-cross section function for spin-independent WIMPs is shown by the black line. The 1σ and 1σ sensitivity projections are shown in green and yellow, with the median sensitivity projection shown by the dotted black line. Sensitivities for previous direct detection studies are shown and labeled (Aalbers et al. 2022)

The data used by the LZ collaboration is captured by the LUX-ZEPLIN detector. The design for the LZ Detector was first proposed in September 2015, with construction beginning in September 2016 and finishing in August 2020. The detector is housed at the Sanford Underground Research Facility in South Dakota, nearly 5,000 feet below the surface. This depth provides an environment that excludes the vast majority of particles that interact strongly with baryonic matter, such as

muons and cosmic rays, while allowing WIMPs, which have interaction rates low enough to easily pass through the intervening earth.

The LZ detector, shown in Figure 1.2, measures nearly 6 meters in height and more than 7.5 meters in diameter. The detector sits within a large tank of water, which is regularly circulated to maintain purity. This water is primarily designed to block radiation from outside sources. The outer detector (OD) uses Photomultiplier Tubes, hereafter PMTs, to measure incoming particles and veto any that interact again in the inner detector. The cryogenic system maintains an inner detector temperature of 80K. The outside of the inner detector is made up of a thin layer of liquid xenon, known as the skin, which provides an additional veto for certain incoming particles (Mount et al. 2017). The methods by which the OD and skin veto events are discussed in § 2.2.

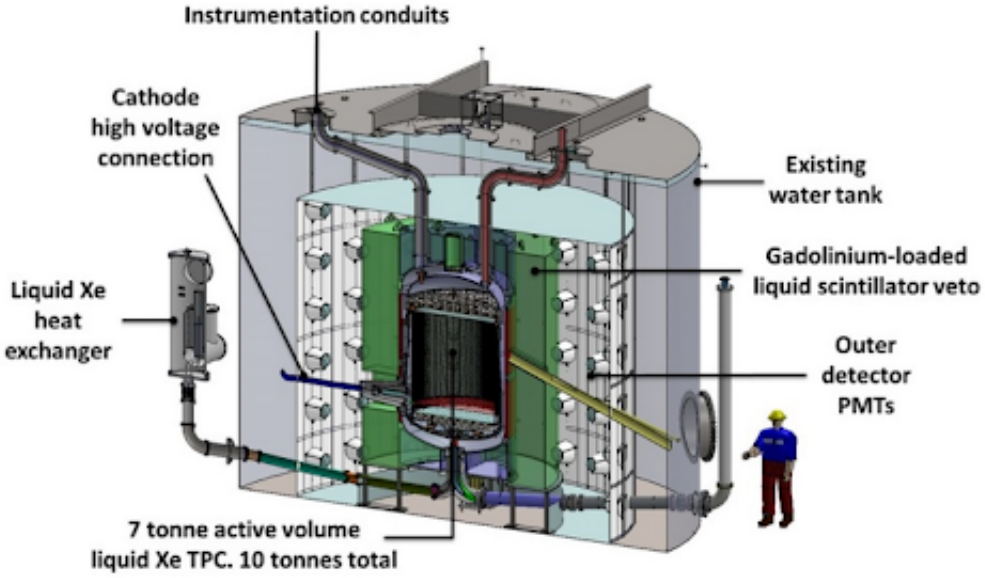

FIGURE 1.2: Model of the LUX-ZEPLIN Detector, with large components labeled and a human for scale (Mount et al. 2017)

The center of the LZ Detector contains the Time Projection Chamber (TPC), which is shown in Figure 1.3. The chamber is roughly 1.5 meters in diameter and and 1.5 meters tall and contains 7 metric tons of ultra-pure liquid xenon (LXe). The top and bottom of the detector both contain an array of PMTs that measure energy of photons and electrons emitted inside the TPC. A cathode at the bottom of the detector, an anode at the top, and field shaping structures embedded in the

walls generate an electric field with a strength of roughly 192 V/cm. The electric field points downwards and is uniform throughout most of the detector (Mount et al. 2017).

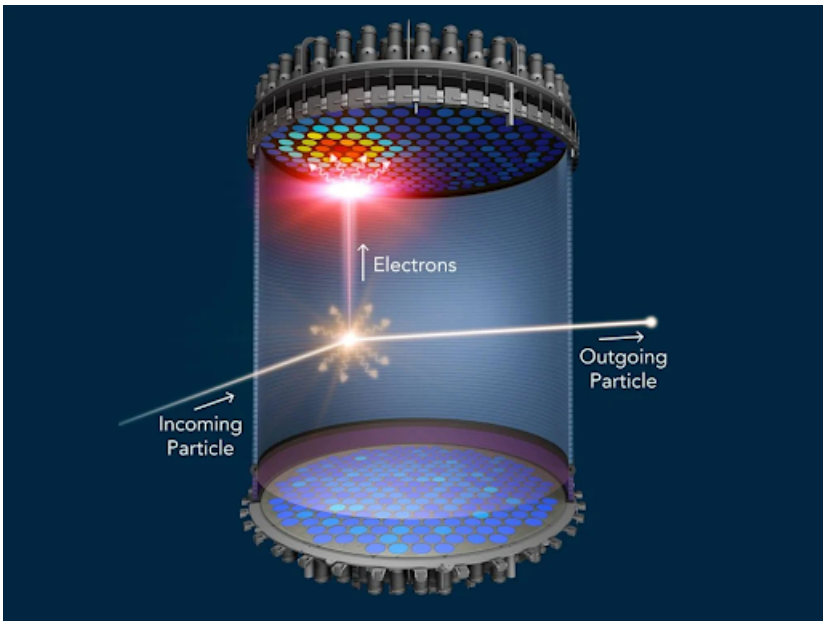

FIGURE 1.3: Diagram of the Time-Projection Chamber collecting data from a particle interaction. In the diagram, a particle enters the detector and deposits some of its energy on a xenon atom, which then emits electrons and photons. Taken from Mount et al. (2017)

Liquid xenon was chosen as the interaction medium for several reasons. Primarily, LXe has been identified as a material with efficient yields for both ionization and scintillation. The large numbers of electrons emitted by the ionization and photons emitted through scintillation allow us to detect lower energy interactions than is possible with other mediums (Mount et al. 2017). Xenon is a noble element, eliminating the need to account for reactions with detector components. The large mass of the xenon nucleus increases the chance of a WIMP passing close enough to interact with the target mass. Finally, LXe was chosen for its stability. While radioactive isotopes of xenon are present in extremely small concentrations, the vast majority of the radioactive events identified during the first observation originated from similarly small argon, krypton, and radon impurities, roughly 80% of all events measured. Meanwhile, only 9% came from Xe decay (Aalbers et al. 2022). The reasoning for the importance of high ionization and scintillation efficiencies as well as large nuclear cross section are discussed in § 1.2.

1.2 Data Collection

The LZ Detector collects data on particle interactions within the TPC by measuring the energy of the ionization and scintillation pulses using PMTs. The photons emitted by the interaction travel outwards at the speed of light and reach the PMTs. The PMTs multiply the signal by a factor of roughly 10^6 before recording the final energy in terms of photons detected, or phd. As the scintillation reaches the PMTs before the ionization, we call the light signal S1.

The electrons that are emitted are subject to the strong electric field and move upwards at roughly 1,500 m/s. The TPC is temperature controlled so that it has a thin layer of Xe vapor just below the PMTs. Due to the high electroluminescence of the Xe vapor, the electrons passing through produce large numbers of photons. These photons are measured by the PMTs as the ionization, or S2 signal (Mount et al. 2017). The shapes and sizes of the two signal types are compared in Figure 1.4.

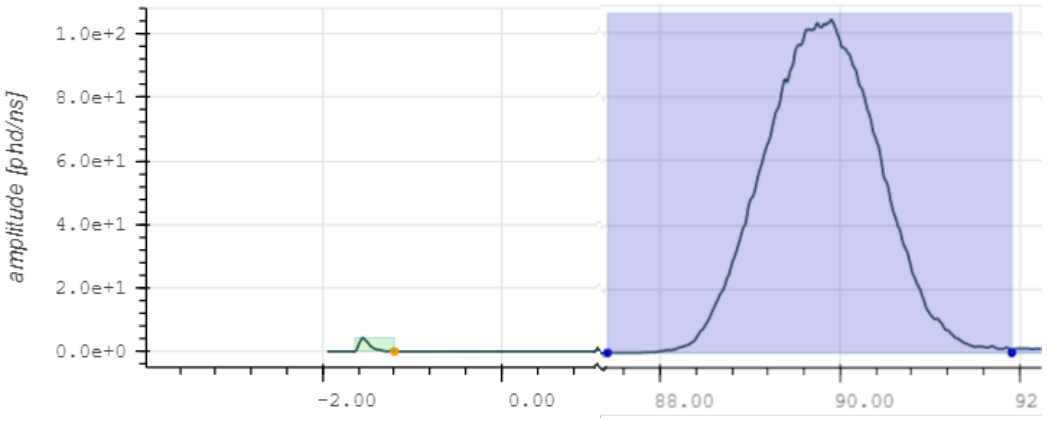

FIGURE 1.4: Comparison of the shape and size of S1 and S2 signals. The S1 signal, seen on the left, is significantly weaker and lasts for less than half a nanosecond. The signal strength quickly peaks before slowly decaying back to zero. The S2 signal on the right is a much stronger signal and lasts 4 ns. The amplitude follows a roughly Gaussian distribution over time.

Particles that pass through the detector can interact with Xe atoms through two mechanisms. When a charged particle passes near a Xe atom, it interacts with the electron shell through the electromagnetic force. We label this type of interaction as Electronic Recoil (ER). As the energy is transferred into the electrons, the

interaction provides enough energy to eject a large number of electrons from the shell. The atomic excitation temporarily creates diatomic xenon, called excimers, which quickly de-excite and emit photons (Akerib et al. 2020).

In contrast, an uncharged particle, such as a WIMP, will not interact with the electrons. Instead, it will be detected if it passes close enough to the nucleus for the weak coupling to cause an energy transfer. In such a Nuclear Recoil (NR) interaction, the energy is transferred into the nucleus of the Xe atom. Thus, some of the energy is converted to heat and the interaction releases less energy in the form of photons than an ER interaction, and an even smaller fraction of the electrons of an ER interaction (Akerib et al. 2020).

Due to the differences in ionization and scintillation efficiency between ER and NR interactions, they can be differentiated by plotting photon energy against electron energy. This creates two distinct bands, one for ER events and one for NR events, as shown in Figure 1.5.

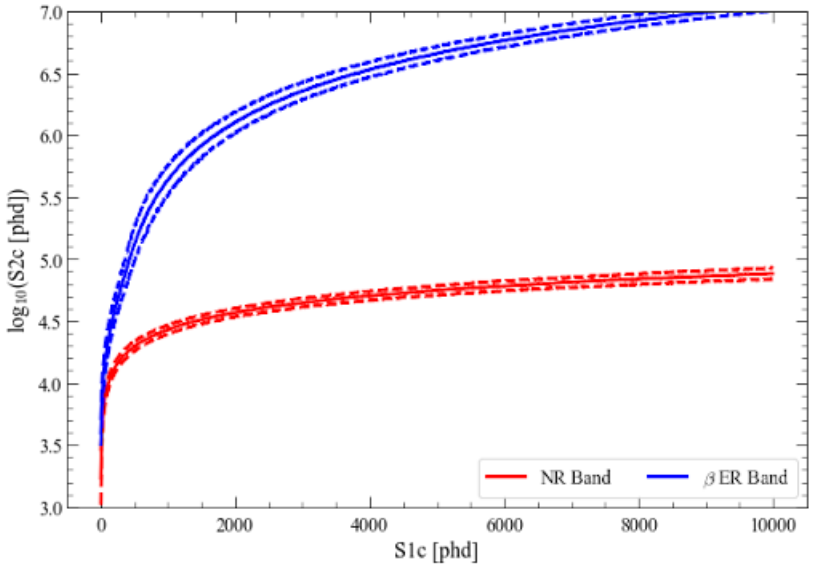

FIGURE 1.5: Plot of the median and 90%-10% probability distribution of the ER and NR bands based on simulation data. S1c and S2c represent the corrected area of the S1 and S2 signal detections, measured in photons detected by the PMTs. The S2 signal is plotted on a log scale, meaning that the S2 strength is several orders of magnitude greater for ER events at all but the lowest energies, leading to easy discrimination.

1.3 The NR Background

A primary challenge faced in the search for WIMP-nucleon interactions is accounting for the NR background. There is a significant number of events, that despite being caused by Electronic Recoil, appear within the NR band. In order to identify whether or not WIMP-nucleon interactions are present in our data, we must compare the NR band detections, shown in Figure 1.6, to the expected number of ER events in the NR band. The total rate of non-dark events in the NR band is known as the NR background. The NR background is primarily made up of two contributors: MSSI events and ER leakage. In addition, the NR background has a large contribution from neutron interactions. As neutrons are uncharged, they generate NR events. These events are primarily removed by the outer detector, and thus are not included in this study.

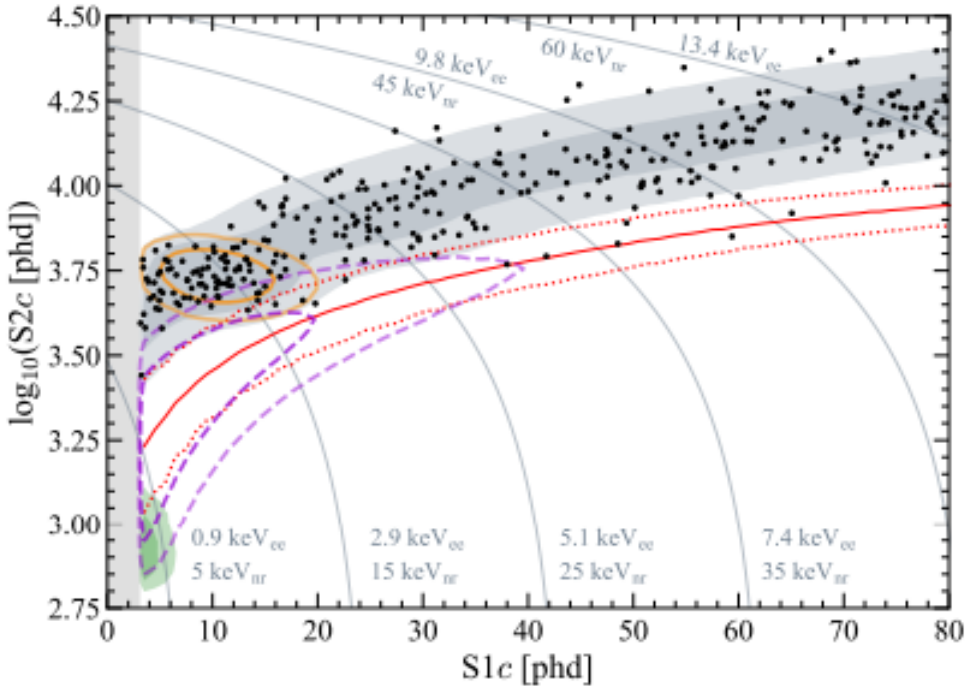

FIGURE 1.6: Plot of event detections from the first 60 days of run time. 12 events are measured within the NR band, between the dotted red lines, with most of the remainder falling towards the middle of the ER band. Some or all of the events in the NR band are likely the result of ER interactions (Aalbers et al. 2022).

1.3.1 MSSI Events

Multiple Scintillation Single Ionization events, often referred to as MSSI, are the result of particles that interact with the LXe multiple times, but are not measured correctly.

When a particle such as a high energy photon interacts with a Xe atom, it may not release all of its energy, instead scattering and traveling as short distance before interacting with another Xe atom. This is known as a double scatter. Because the incoming photon travels at the speed of light, the two interactions occur near instantaneously. Therefore, the photons emitted by the two interactions indistinguishable and generate a single, larger S1 signal. Thus, events are identified as double scatters by the presence of two separate S2 signals.

MSSI events occur when the scintillation of both events is detected, but the ionization of one event is lost. This phenomenon stems primarily from the non-uniformity of the TPC's electric field, which causes an electron's path to intersect with a wall and not reach the PMTs. Figure 1.7 shows the Reverse Field Region (RFR) present below the cathode. Additionally, while the electric field shaping structures in the TPC walls are closely packed, there is a nonzero separation between them. This creates small inconsistencies near the wall, where the space between the field shapers results in an inconsistent electric field. These electric field dead zones near the walls of the TPC are displayed in Figure 1.8.

When a scatter occurs below the cathode, the electrons are released as normal. However, as the electric field below the cathode points upwards, the electrons are forced to the bottom of the TPC. Because of this, the electrons do not pass through the Xe vapor and are not measured by the PMTs.

For scatters that occur very close to the walls of the detector, electrons can become caught by the dead zones. The electric field in the red regions of Figure 1.8 push electrons away from the wall, towards the drift region. As the electron moves upwards, it reaches a blue dead zone, with an electric field pointing the other direction, pushing the electron back towards the wall. This creates an oscillatory path for the electron, with some paths intersecting the wall. The electrons following these paths will not reach the PMTs.

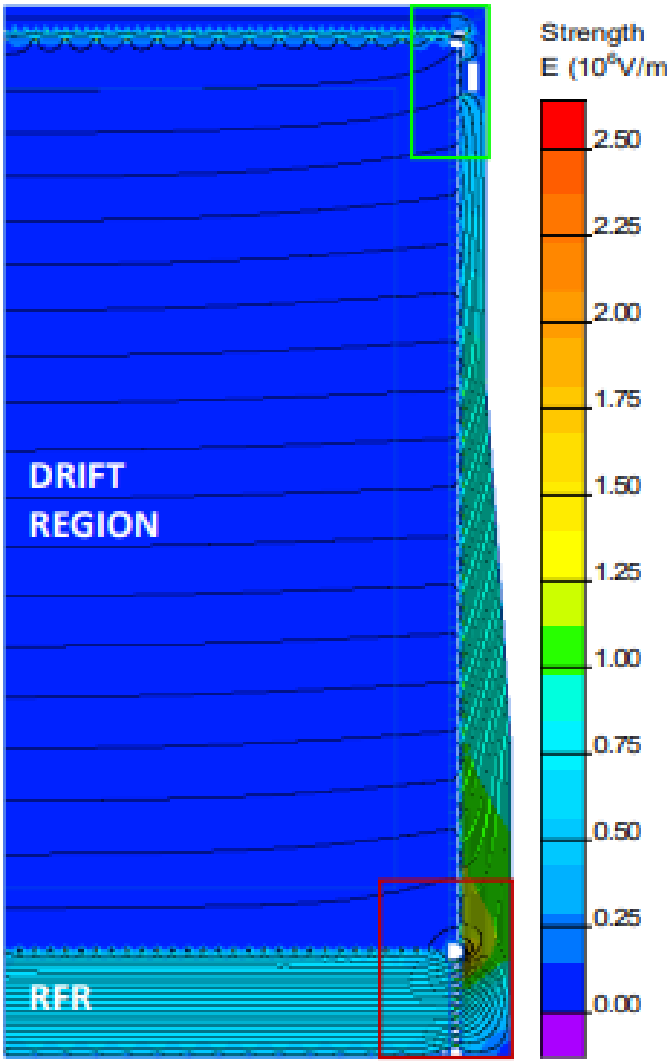

FIGURE 1.7: Diagram of the electric field strength relative to location in the detector, with radius from the center plotted on the x-axis. Potential contours are shown in black. The electric field is significantly stronger and points the opposite direction below the cathode, with this region being designated the Reverse Field Region (Mount et al. 2017).

As Double scatters are identified by the double S2 signal, an MSSI, which only measures one S2, will be misread as a single scatter. As the scintillation of both scatters are measured, this single scatter will have an S1 signal equal to the S1 sum of the two scatters. This event moves to the right from the ER band displayed in Figure 1.5, potentially landing within the NR band and becoming part of the NR background.

The double scatters that can be read as MSSI come from two primary sources. The

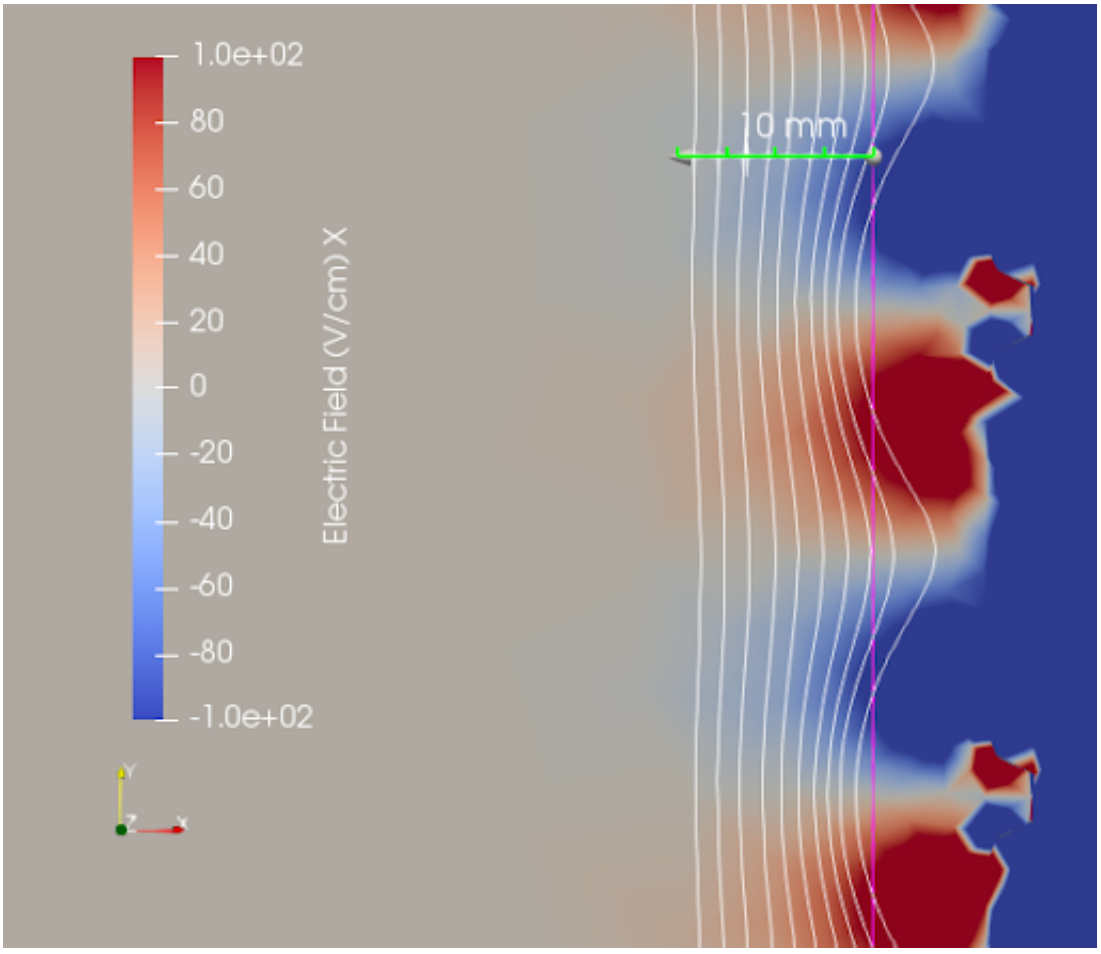

FIGURE 1.8: Model of the electric field strength relative to the drift region near the wall of the detector, with radius from the center plotted on the x-axis and height on the y-axis. This region is significantly enlarged to show the small fluctuations clearly. Electric field lines are shown in white, with dead zones in dark blue (Plot created by Reed Watson).

more well understood source of MSSI is the radioactive decay of atoms within the LXe. As the few radioactive isotopes in the sample decay, they emit γ photons with high enough energy to create a double scatter. Previous research has estimated the xenon-based MSSI rate to be around 1.7 events below 600 phd for the first 60 days of run time (Rischbieter 2022). Due to the low rate and the fact that many of the MSSI will fall outside of the NR band, their contribution to the NR background is expected to be low.

The second potential source of MSSI is from detector components. Detector components are manufactured to be highly radiopure. Nevertheless, there is likely to

be a small number of double scatters that originate from detector components. Component-based double scatters have an increased likelihood of being measured as MSSI as a result of their proximity to the electric field inconsistencies. Because of this, we expect cathode-based MSSI due to the RFR and wall-based MSSI due to the dead zones. The rate of component based MSSI is not well constrained, but is expected to be low.

1.3.2 ER Leakage

Apart from MSSI, the other large contributor to the NR background is leakage from the ER band. As a natural result of uncertainties in particle interactions as well as signal detection, ER events regularly fall outside of the ER band, roughly following a Gaussian distribution. The distribution means that ER events can be measured with an S1 and S2 that are characteristic of an NR interaction. This effect is especially pronounced at low energies, when the ER and NR bands are close together. Because the rate of ER events is significantly higher than MSSI, we expect ER leakage to be by far the largest contributor to the NR background.

CHAPTER 2: Computational Methods

The primary goal of this project is to identify the NR background rate for a wider S1 range than previously calculated. The first results paper published in June 2022 included events with S1 areas up to 80 phd, which are shown in Figure 1.1. This cutoff is reasonable for the assumed spin-independent WIMP-nucleon interaction model, for which most interactions fall at low energies. In this project, we create a model for the NR background for S1 events up to 600 phd. Using the expanded model, the LZ collaboration will be able extend the range of the WIMP search, increasing the sensitivity for WIMP-nucleon interaction models with higher rates of high energy events. The alternative interaction models are discussed further in Section 2.1. In order to create the model for the NR background rate, we performed an analysis of Near Miss MSSI events, as well as simulations to calculate the leakage of ER and xenon-based MSSI into the NR band.

2.1 WIMP-Nucleon Interaction Operators

Though the first set of data analysis was handled with the assumption that the interaction between dark matter and xenon nucleons is spin-independent, However, there are several competing models of these interactions. These interaction models were created using a simplified extension of the standard model in the non-relativistic case that includes dark matter and a particle to mediate the interaction between DM and standard model particles (Goodman & Witten 1985).

Using the extension of the standard model, researchers generated linear operators in terms of basic invariants under four symmetries. These symmetries are of three-dimensional momentum transfer, relative velocity of the particles, and the spin of the WIMP and nucleon, respectively. These calculations resulted in 14 independent linear operators for interactions between spin 1/2 WIMPs and nucleons, shown in Figure 2.1. Operators 17 and 18 only apply to spin 1 WIMPs from Baum et al. (2018), which we did not include in our study. This left the

Operator	Type of spectrum
$\hat{\mathcal{O}}_1 = \mathbb{1}_\chi \mathbb{1}_N$	A
$\hat{\mathcal{O}}_3 = i\hat{\mathbf{S}}_N \cdot (\frac{\hat{\mathbf{q}}}{m_N} \times \hat{\mathbf{v}}^\perp)\mathbb{1}_\chi$	B
$\hat{\mathcal{O}}_4 = \hat{\mathbf{S}}_\chi \cdot \hat{\mathbf{S}}_N$	A
$\hat{\mathcal{O}}_5 = i\hat{\mathbf{S}}_\chi \cdot (\frac{\hat{\mathbf{q}}}{m_N} \times \hat{\mathbf{v}}^\perp)\mathbb{1}_N$	B
$\hat{\mathcal{O}}_6 = (\hat{\mathbf{S}}_\chi \cdot \frac{\hat{\mathbf{q}}}{m_N})(\hat{\mathbf{S}}_N \cdot \frac{\hat{\mathbf{q}}}{m_N})$	B
$\hat{\mathcal{O}}_7 = \hat{\mathbf{S}}_N \cdot \hat{\mathbf{v}}^\perp \mathbb{1}_\chi$	A
$\hat{\mathcal{O}}_8 = \hat{\mathbf{S}}_\chi \cdot \hat{\mathbf{v}}^\perp \mathbb{1}_N$	A
$\hat{\mathcal{O}}_9 = i\hat{\mathbf{S}}_\chi \cdot (\hat{\mathbf{S}}_N \times \frac{\hat{\mathbf{q}}}{m_N})$	B
$\hat{\mathcal{O}}_{10} = i\hat{\mathbf{S}}_N \cdot \frac{\hat{\mathbf{q}}}{m_N} \mathbb{1}_\chi$	B
$\hat{\mathcal{O}}_{11} = i\hat{\mathbf{S}}_\chi \cdot \frac{\hat{\mathbf{q}}}{m_N} \mathbb{1}_N$	B
$\hat{\mathcal{O}}_{12} = \hat{\mathbf{S}}_\chi \cdot (\hat{\mathbf{S}}_N \times \hat{\mathbf{v}}^\perp)$	A
$\hat{\mathcal{O}}_{13} = i(\hat{\mathbf{S}}_\chi \cdot \hat{\mathbf{v}}^\perp)(\hat{\mathbf{S}}_N \cdot \frac{\hat{\mathbf{q}}}{m_N})$	B
$\hat{\mathcal{O}}_{14} = i(\hat{\mathbf{S}}_\chi \cdot \frac{\hat{\mathbf{q}}}{m_N})(\hat{\mathbf{S}}_N \cdot \hat{\mathbf{v}}^\perp)$	B
$\hat{\mathcal{O}}_{15} = -(\hat{\mathbf{S}}_\chi \cdot \frac{\hat{\mathbf{q}}}{m_N})[(\hat{\mathbf{S}}_N \times \hat{\mathbf{v}}^\perp) \cdot \frac{\hat{\mathbf{q}}}{m_N}]$	B
$\hat{\mathcal{O}}_{17} = i\frac{\hat{\mathbf{q}}}{m_N} \cdot \boldsymbol{\mathcal{S}} \cdot \hat{\mathbf{v}}^\perp \mathbb{1}_N$	B
$\hat{\mathcal{O}}_{18} = i\frac{\hat{\mathbf{q}}}{m_N} \cdot \boldsymbol{\mathcal{S}} \cdot \hat{\mathbf{S}}_N$	B

FIGURE 2.1: Quantum Mechanical Operators for WIMP-nucleon interactions. Operators 2 and 16 are linear combinations of other operators and thus are not shown (Baum et al. 2018).

spin-independent operator 01 and the spin-dependent operators 03 through 15 for leakage analysis.

2.2 Near Miss MSSI Analysis

We found the total component-based MSSI rate for events within the target energy range using data from the first observing run of the LZ detector. The Near Miss MSSI search identified Near Miss MSSI events, which closely match the circumstances that would result in an MSSI, but are measured correctly. The events we studied were therefore double scatter ER interactions with a detection near the wall or cathode of the TPC.

The data used in the Near Miss MSSI Search was taken from the first observing run of LZ. This consisted of 60 live days of data collection between between December 2021 and April 2022. Through the use of an algorithm that identifies S1 and S2 signals by their shape and size, we selected all events with a single S1 peak and two S2s, characteristic of double scatters. This initial data set contains more than 3 million events and is displayed in Figure 2.2.

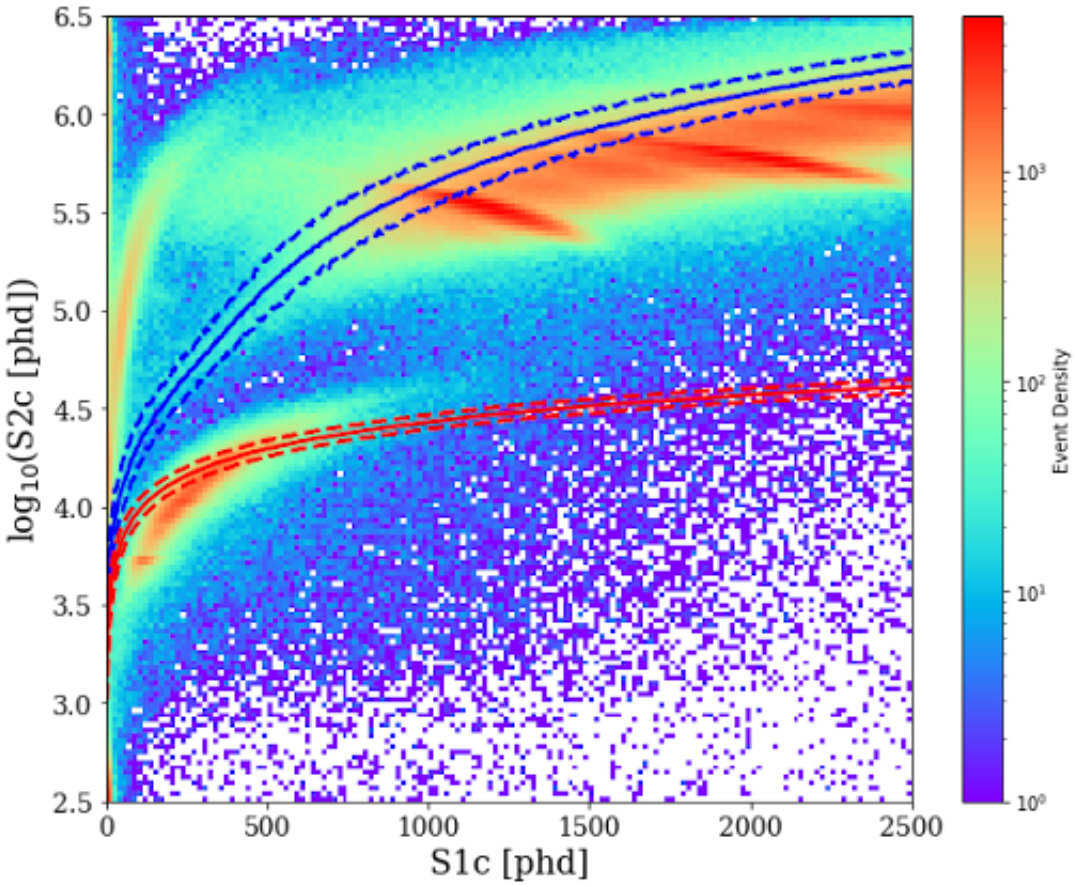

FIGURE 2.2: Distribution of S1 and combined S2 area of all events included in this study. ER and NR bands are overlaid in blue and red, respectively. As the events are double scatters, their reconstructed S1 and S2 areas are each roughly double what they would be for single scatters, causing an offset from the ER and NR bands. Most events fall near the ER and NR bands, though there are many events outside these bands, particularly at lower energies.

2.2.1 Data Cuts

The large quantity of events included in the study mean that it is impossible to perform manual analysis on all data points. In order to deal with this, we implemented several standard selection criteria, also known as cuts, that are used in the WIMP search. Any MSSI that would be excluded through these cuts has no impact on the accuracy of the WIMP search. Because of this, we are able to reduce the size of our data set and increase the accuracy of our Near Miss MSSI count by eliminating all double scatter events that fail the standard cuts.

The first cuts we performed were a skin cut and an outer detector cut. These cuts excluded all events with a simultaneous detection in the skin layer or OD. Due to dark matter's extremely low rate of interaction with baryonic matter, we have yet to conclusively detect even a single WIMP-nucleon interaction, the chance of a WIMP interacting with the xenon in the skin or OD as well as inside the TPC is effectively zero. Therefore, all events with associated skin and OD scatters are ignored when searching for WIMPs.

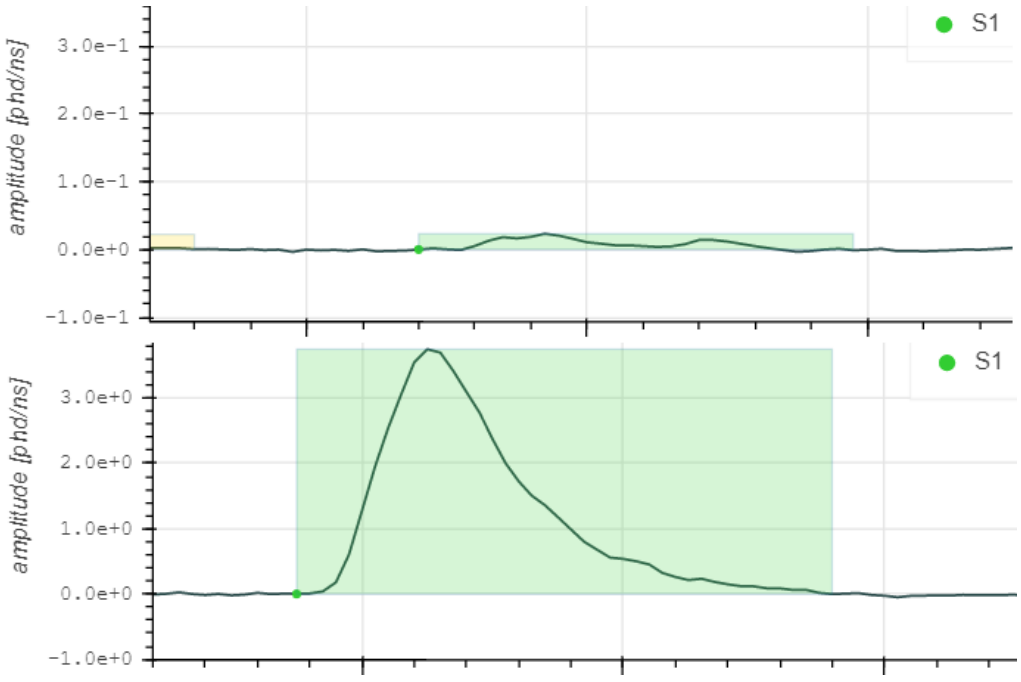

FIGURE 2.3: Comparison of random noise incorrectly marked as S1 (top) to an expected S1 signal (bottom). Taken from a single scatter event using the LZ event viewer. Note that the amplitude scale for the noise based S1 has been magnified 10x.

The next set of cuts we used were quality cuts for the S1 and S2 detections. The algorithm we use uses difference of Gaussian filters and decision trees based on parameters such as rise time and PMT coincidence, as well as a hard cutoff for signals below 3 phd to determine whether a signal is S1, S2 or neither (Williams 2022). Additionally, it marks events with whether or not the signal is very likely to be real based on the shape and size of the S1 and S2 signals. While low confidence events are useful for some aspects of analysis, this method can identify random noise as S1 signals, an example of which is compared to a true S1 in Figure 2.3. The WIMP search, and thus the Near Miss MSSI search, only performs analysis on events that are very likely to be real. The S1 and S2 quality cuts exclude all events that are faint or of an irregular shape, and thus have low confidence. After taking the S1 and S2 quality cuts, we are left with events with a high likelihood of being real.

The final standard cut we used was a fiducial volume cut. Due to the low interaction rate of DM, we can use the skin and OD to veto many non-dark particles. However, as the path length of certain particles, such as gamma photons (γs) and neutrons, is on the order of 10 cm between interactions, it is possible for these particles to interact just outside the skin and again just inside the TPC.

The edges of the detector are also exposed to radiation from material surrounding the detector than the inner region of the TPC due to the self-shielding of the LXe. LXe's high density mean that any high interaction rate particles passing through the detector will quickly interact with a xenon atom. Therefore, few incoming particles will pass through a significant length of LXe. As the majority of particles that pass through the TPC originate from outside the detector or from the radioactive decay of impurities in its components, the center of the TPC has a much lower event rate, as seen in Figure 2.4.

In order to reduce the rates of missed double scatters and total non-dark interactions, we constrain the data used in the WIMP search to interactions within the fiducial volume (FV). The FV is a cylindrical volume at the center of the TPC with a radius of roughly 70 cm and a height of roughly 130 cm and contains roughly 5.6 metric tons of LXe. Within this volume, the chance of a γ or neutron's second

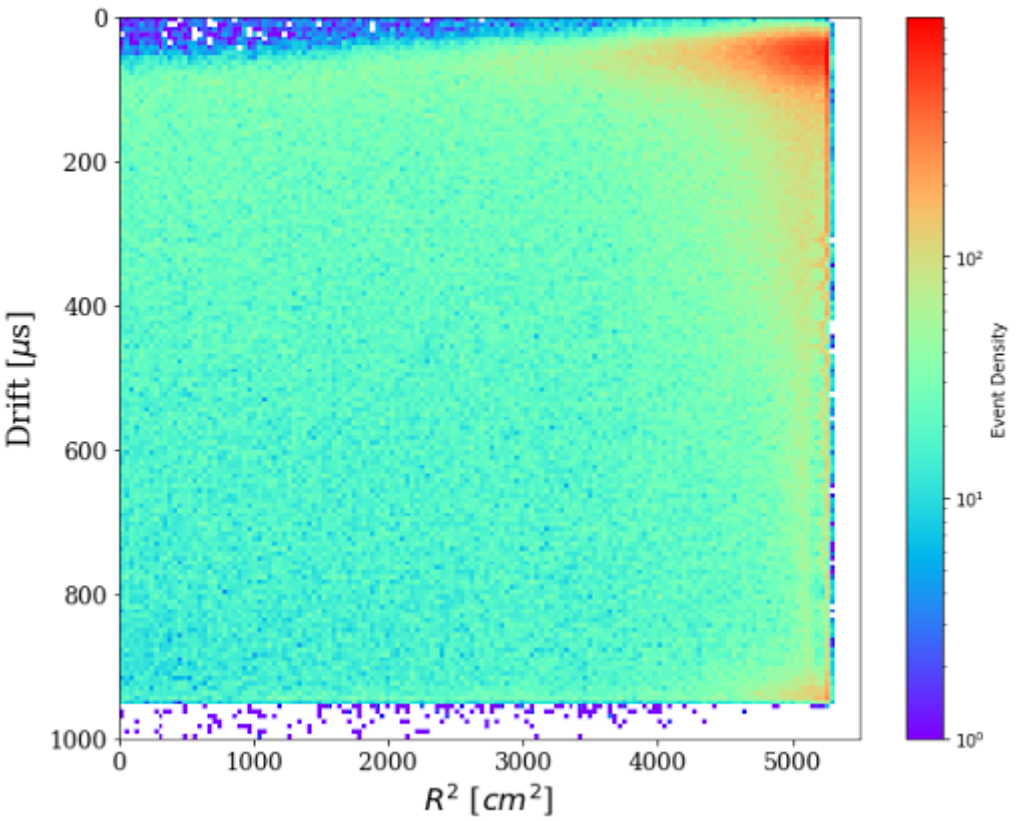

FIGURE 2.4: Event density of double scatters compared to location in the detector. Horizontal position is shown as R^2 to remove bias as a result of larger radii containing a larger volume.

interaction being missed is much lower, thus lowering the noise level (Mount et al. 2017).

While the FV cut is simple to implement for the WIMP search, simply by removing all events that occur outside the fiducial volume. However, due to the nature of the double scatters in our data, we created a more complex FV cut that included the Near Miss MSSI events we intended to study.

The FV cut we selected generally performs the same task as the standard FV cut, with one primary exception. For a double scatter to pass our FV cut, only one of its scatters must occur within the FV. By including events with a scatter outside the FV, we hope to capture double scatters with a xenon interaction near the detector walls and cathode as these are similar to the double scatters that result in MSSI detections. The data that passes the FV cut is shown in Figure 2.5. More in-depth analysis of the FV cuts we considered is provided in Appendix A.

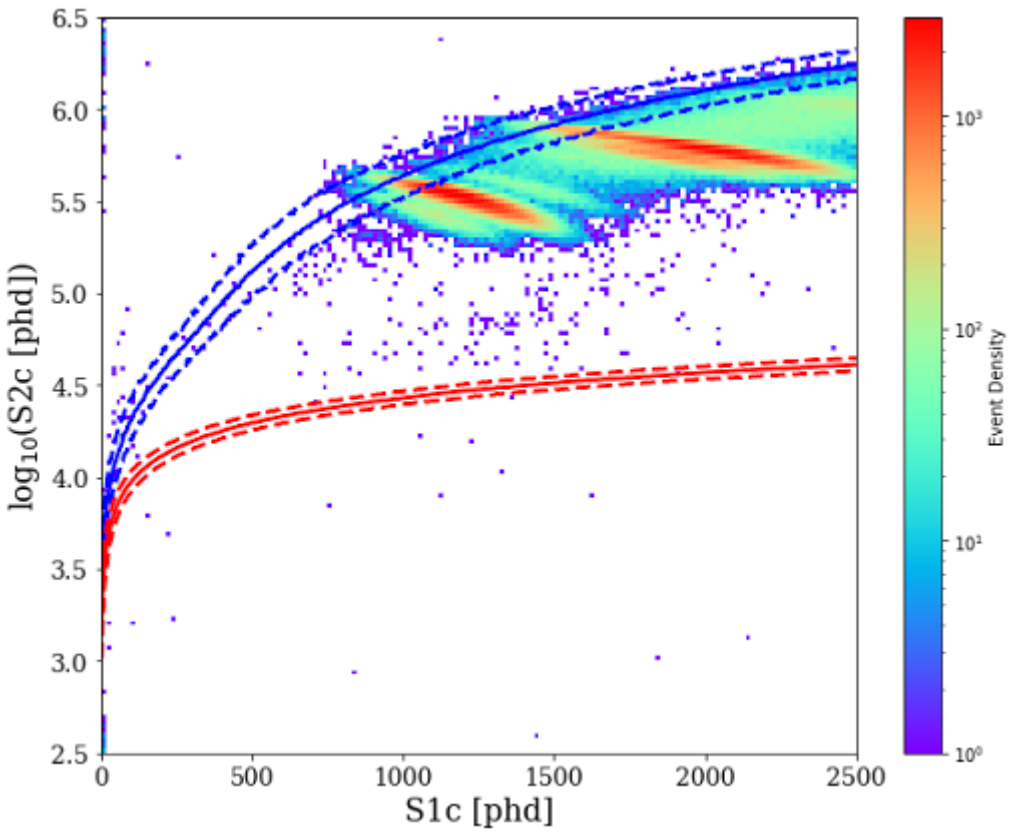

FIGURE 2.5: Plot of double scatters that have passed all standard data cuts. There seem to be false detections remaining at the low end the of S1 area axis, but most of the noise has been eliminated.

In addition to the standard cuts we used to fit with the WIMP search, we implemented a series of cuts designed to isolate Near Miss MSSI events that threaten the WIMP search. Although there were a large number of events remaining in our data set, very few of them have the potential to leak into the WIMP region if they were to become MSSI. Thus, we used a xenon decay cut and a diagonal cut to create a manageable data set for manual processing.

Although our research primarily focused on events with S1 areas below 600 phd, due to the greater concentration of MSSI at higher energies, we extended the range of our S1 cut to increase the sample size. An issue we faced with the extension was that, above 700 phd, we begin to run into xenon decay based MSSI. The left overdensity of double scatters seen in Figure 2.5 is caused by the decay of Xe-127, and the right is caused by Xe-129. In order to identify the detector component-based MSSI rate, we must exclude these events from our data set, and set the upper

limit of the xenon decay cut to 700 phd. Due to the high energy requirement of a particle to generate a double scatter, it is highly unlikely for double scatters with low S1 area to be real. Therefore, we additionally cut events with S1 areas below 30 phd.

The final cut we made was a diagonal cut to exclude any remaining false detections. As our study is built to measure the rate of ER double scatters, we can eliminate all events a significant distance from the ER band. To do this, we built a diagonal cut centered on the ER band median and extending 0.5 above and below, which translates to a factor of $\sqrt{10}$ as S2 is plotted in in log space. Following this series of data cuts, we were left with the 61 events shown in Figure 2.6.

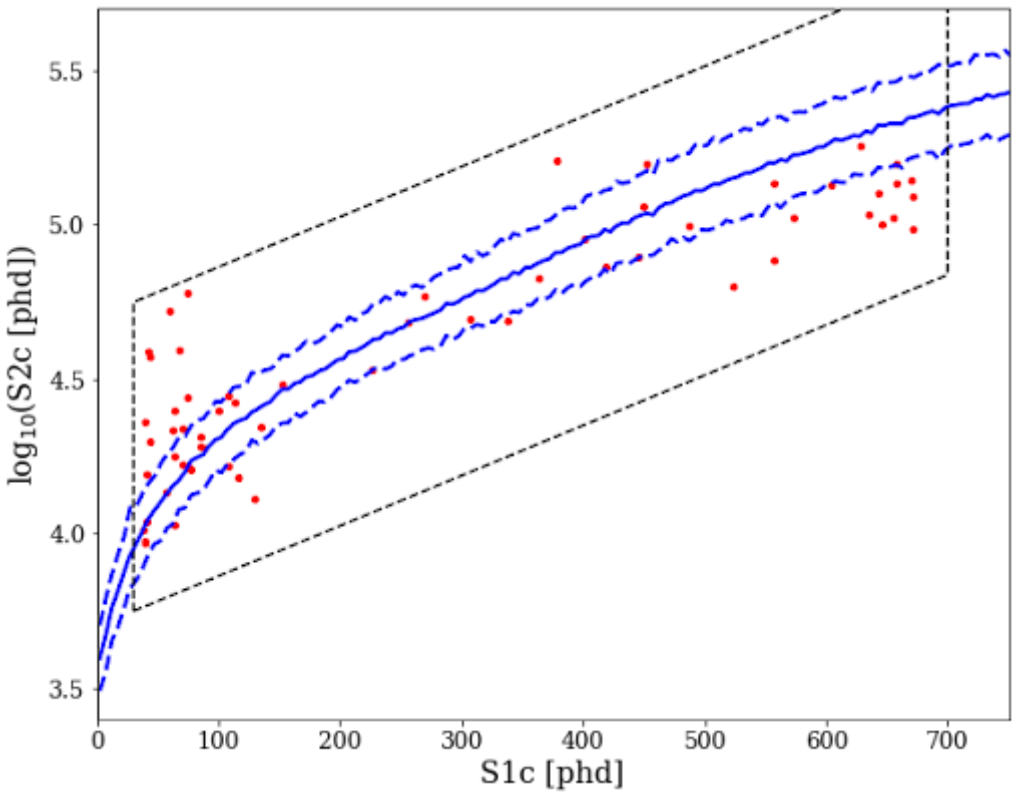

FIGURE 2.6: 61 double scatters that passed all quality cuts. The xenon and diagonal cuts are shown in black and the ER band is shown in blue. There are two primary groupings of double scatters, one with lower energies and one with high energies.

2.2.2 Hand Scanning

The final step of the data processing was to manually analyze the event waveforms to remove any remaining false double scatters. Because double scatters are automatically identified by computer analysis, unexpected signals that are easily identifiable by a human may be misread. We used the LZ event viewer to check each of the remaining events against the expected form of double scatters. The full waveform of an event seen in the event viewer is displayed in Figure 3.5.

The manual scanning we performed was primarily focused on the S1 signals. The energy captured in an S2 detection is several orders of magnitude larger than that of an S1, so the chance of a false positive or missed S2 is extremely low. On the other hand, S1 signals are weak enough that they can be confused with detections of a few stray photons by the algorithm.

If an S1 detection is missed, the primary events that appear as double scatters are pileup events. These occur when two separate particles interact with the liquid xenon in close succession. This generates two S1 pulses and two S2 pulses, which in this case are read as a single S1 and two S2. Through this analysis, we identified the S1 signals that had been missed by the algorithm and excised them from the data. An example of an incorrectly marked pileup event is shown in Figure 2.7.

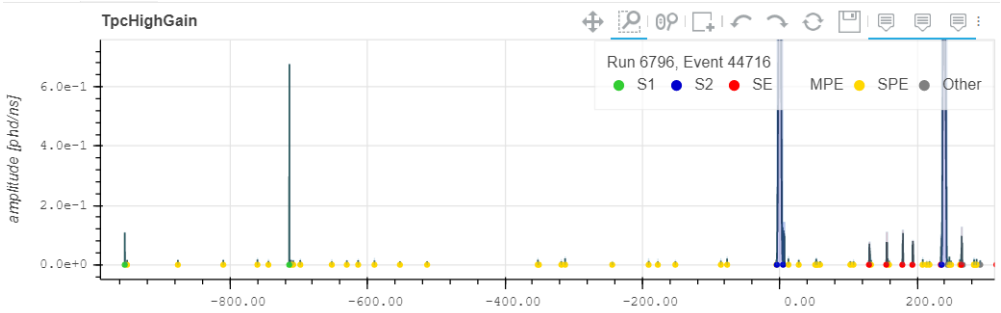

FIGURE 2.7: The waveform of a pileup event that was incorrectly marked as a double scatter. Due to the small size of the first S1 signal, it was not properly identified.

After the completion of the hand scanning, we were left with a data set containing only true double scatters. The number of events removed with each step and the cut efficiency are shown in Table 2.1.

Data Cut	Events Removed	Efficiency [%]
Skin and OD Cuts	1155244	35.45
S1 S2 Quality Cuts	1470160	69.89
FV Cut	250349	39.52
Diagonal Cut	383035	99.98
Hand Scanning	36	59.02

TABLE 2.1: Events removed in each step of the data selection process. Both the absolute number of events and the percentage of remaining events were removed is given. While the S1 and S2 quality cuts removed the most events, the Diagonal cut had by far the greatest efficiency.

2.3 MSSI and ER Leakage Rate

Next, we calculated the rate at which MSSI and ER events are found within the WIMP-nucleon interaction region of S1-S2 space using simulated data of the three types of detections. The rate was calculated by first generating WIMP-nucleon specific bands, similar to the NR band seen in Figure 1.5. Then we calculated the rate at which ER and MSSI events fall in and below the WIMP-nucleon band to identify the total number of leakage events.

2.3.1 WIMP-nucleon Recoil Bands

Although there are 16 operators that could potentially govern WIMP-nucleon interactions, many of them have low rates of high energy events. As the first results paper calculated leakage rates for low energy interactions, we found it most important to calculate the leakage rates for interaction models with significant event rates at higher energies. In order to identify the most important operators to study, we used simulated signals of WIMP-nucleon interactions with different operators and masses. We plotted the ratio of events with S1 areas of 300 phd to those with 50 phd in Figure 2.8 and selected the operators with the greatest ratio for study, which came out as operators 03, 06, 10, 13, and 15.

Using the Noble Element Simulation Technique detailed in Szydagis et al. (2013), which generates light and charge yields based on input energy, we simulated new

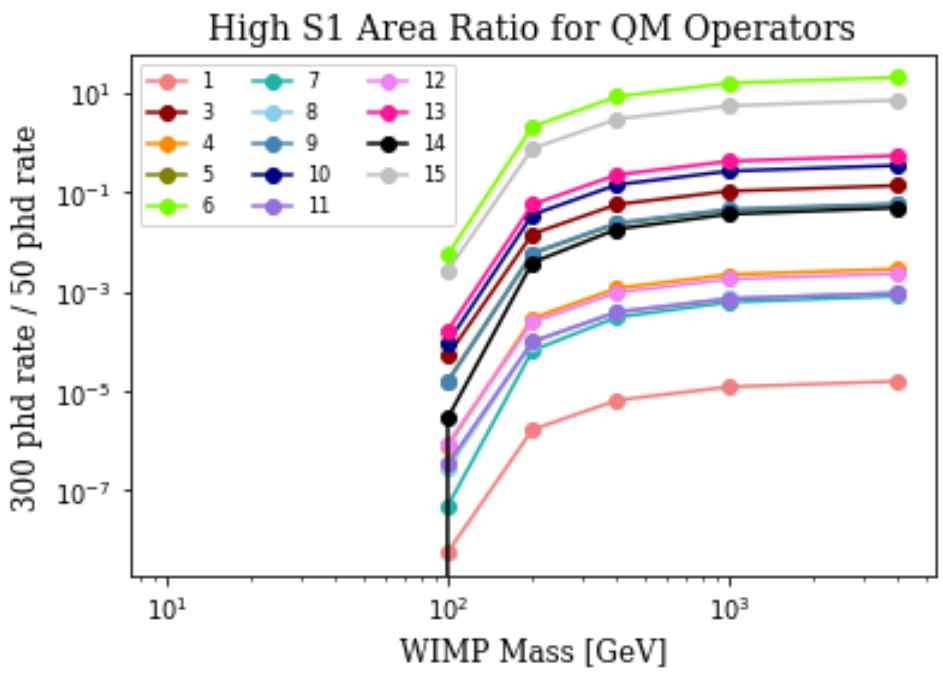

FIGURE 2.8: Ratio of events with 300 phd S1 detection to 50 phd S1 detection. Ratio rises for higher mass WIMPs, and is consistently highest for operator 06, followed by operators 15, 13, 10, and 03.

data consisting of 2 million WIMP-nucleon interactions for each of the 5 operators identified above for WIMP masses of 400 GeV and 4000 GeV. Additionally, we simulated data for the spin independent operator 01 and its positive and negative uncertainty levels. Due to an issue with the code, the positive and negative uncertainty of the spin-independent model were simulated by Dr. Greg Rischbieter.

We used band maker code to calculate the mean of the distribution and the 10%-90-% confidence levels as a function of S1 area. The 10%-90% confidence levels are bands of the 10th and 90th percentile for S2 area based on S1 area. The 10%-90% confidence levels for the ER and flat NR bands are shown as dashed lines in Figure 1.5. Unfortunately, there was an error with the simulated data for operator 15 and operator 06 for 4000 GeV mass WIMPs. This error persisted across multiple simulations and prevented the bands from being created. Thus, these WIMP-nucleon interaction models had to be excluded from analysis. Bands for the other operators are displayed in Appendix B.

2.3.2 ER Leakage Calculations

We used the same simulation as was used for the NR data to generate 10 million ER events from which we calculated the leakage rate. As the ER band is much closer to the NR band at low energies and separates significantly for higher energy interactions, the ER simulation simulated events with S1 areas up to 200 phd. Additionally, as we wished to find the leakage for different values of S1 area, we had to simulate a large number of ER events to calculate the leakage accurately. The simulated data is plotted against the NR bands in Appendix B.

To calculate the leakage rate, we counted the number of events that fell below the 90% confidence line and the number below the band median for the NR band. By separating the events into 5 phd wide boxes, we then found the number of events below the NR band as a function of S1 area, and calculated the rates by dividing by the total number of events in the S1 range. The results are discussed in Section 3.

2.3.3 MSSI Leakage Calculations

MSSI events were simulated using a custom simulator built by Dr. Greg Rischbieter that based on the Compton scattering of gamma photons with an input energy spectrum. As the processes that generate MSSI are more complicated than ER or NR signals, this simulation is much more computationally rigorous. Thus, he simulated 3 million events up to a maximum S1 area of 600 phd. The data from this simulation is plotted against the NR bands in Appendix B.

The MSSI leakage calculation differed in two primary ways from the calculation for ER events. The irregular distribution of MSSI necessitated the calculation of events between the 10% and 90% confidence levels rather than leakage below. Additionally, the low expected leakage rate meant that an accurate calculation of the total rate is more important than the S1 dependent rate that was found for the ER leakage. The results are discussed in Section 3.

CHAPTER 3: Results and Analysis

3.1 Near Miss MSSI Search

After the data processing described in Section 2.2, the data set contained 25 Near Miss MSSI events with S1 areas between 30 phd and 700 phd. The data are shown in S1-S2 space in Figure 3.1. Figure 3.2 displays the relative positions of the recoil events for each double scatter, with the two scatters for each event connected by a gray line.

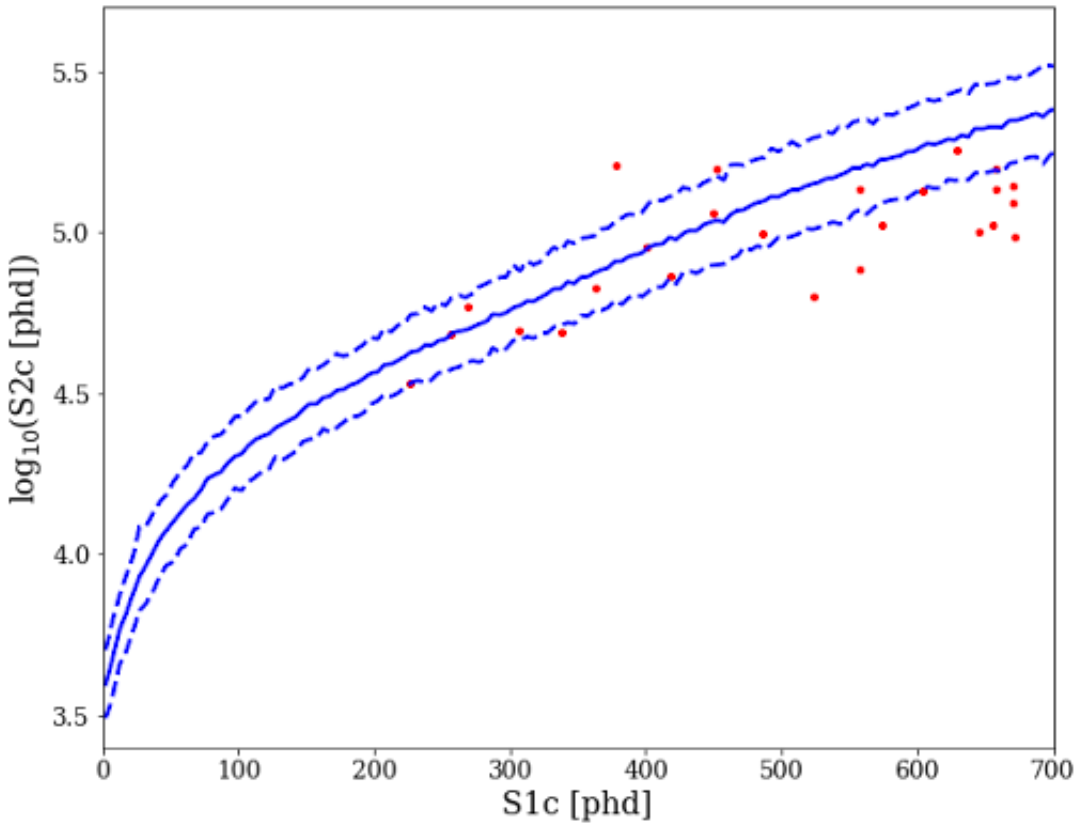

FIGURE 3.1: Near Miss MSSI events displayed with ER band shown in blue. Note that the events are more concentrated at higher energies, with none below 200phd.

In Figure 3.2, there is the distinct lack of Near Miss MSSI near the cathode at the bottom of the detector. Using our assumption that the rate of Near Miss

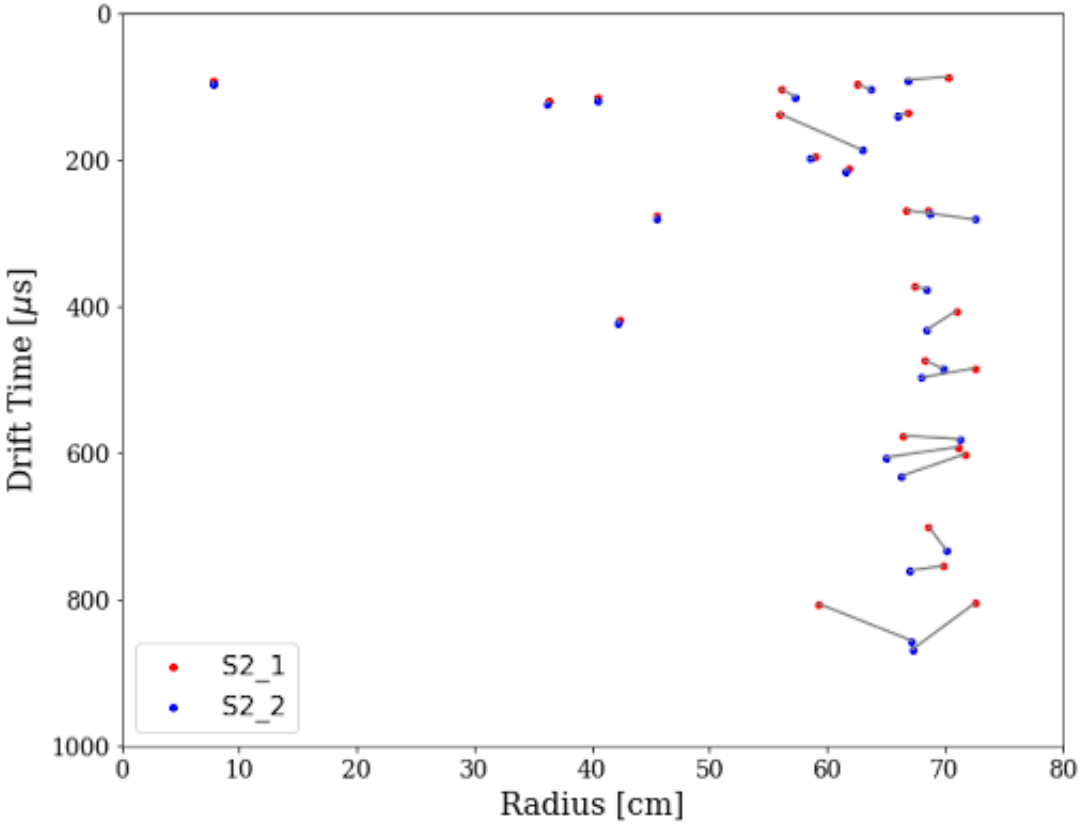

FIGURE 3.2: Near Miss MSSI plotted by their location in the TPC. Drift time is roughly proportional to vertical depth and is plotted in reverse so that events near the top of the detector are shown at the top of the plot. There are many events near the outer walls but virtually none near the cathode.

MSSI events is similar to the rate of true MSSI events, we expect the rate of cathode-based MSSI to be effectively zero. Thus, it is not necessary to account for cathode-based MSSI in the WIMP search.

In contrast, Figure 3.2 shows roughly 15 Near Miss MSSI near the outer wall of the TPC. Using the same assumption for these, we should expect the wall-based MSSI rate to be on the order of 10 events. However, when we compared this to the data from the first observing run of the LZ detector, we did not see what we predicted. In fact, we see zero events that are consistent with wall-based MSSI.

Based on the apparent conflict between the calculated and observed wall-based MSSI rates, we must conclude that our assumption breaks down for wall-based MSSI. Although there are a large number of double scatters near the detector

walls, electrons are not becoming trapped in pockets with weak electric field at the rate we expect.

We theorize that the unexpectedly low MSSI rate is the result of a charge buildup on the inner walls of the TPC. As some of the electrons emitted due to ER interactions build up on the TPC walls, they would generate a slight electric field directed towards the detector walls. This field would cause electrons emitted in the weakened electric field regions to be pushed to the interior of the detector and be detected as normal. If this theory is correct, the MSSI rate would be kept low at the cost of small errors in measured position. Ultimately, we conclude that the electric field model must be refined more to deduce the cause of the low MSSI rate.

3.2 Pileup Events

During hand scanning for the Near Miss MSSI search, we were surprised by the number of pileup events we identified just above the cathode. While pileup events are not too uncommon, we usually expect them to follow a similar distribution to the single scatters that constitute them. However, after correcting the data to accurately reflect the drift time of the scatter that was measured accurately, this clearly is not the case. Every event occurs at the same depth, with a drift time of 950 μs as seen in Figure 3.3, and thus is located at the cathode. Due to the overdensity of pileups we observe, we expect there is be a source of pileup events originating at the bottom of the detector.

Apart from the shared location, these pileup events have several similarities. We reconstructed the total energies using the equation $E = W(S1/g1 + S2/g2)$. In this case, W is the energy to release one quanta in the form of an electron or photon, 0.0135 keV, and g1 and g2 are the rates at which a single photon or single electron are converted into phd by the PMTs, 0.114 phd/photon and 47.1 phd/electron respectively as used in Aalbers et al. (2022). We found the pileup events' energy to be significantly lower than for the double scatters as shown in Figure 3.4. The horizontal displacement between the scatters is below 2 cm for all pileup events, which is likely a result of the poor position reconstruction resolution

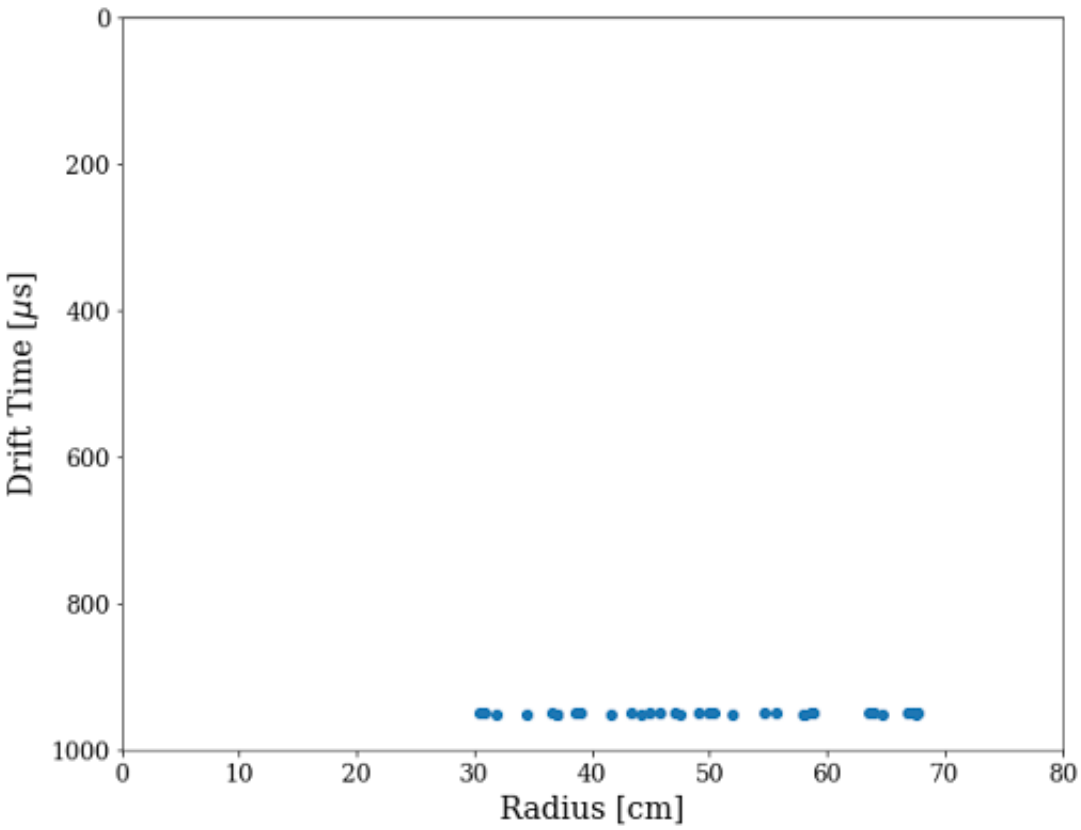

FIGURE 3.3: Pileup event position using corrected drift time. All drift times fall between 950 μs and 952 μs. This is the depth of the cathode and falls outside the fiducial volume.

(Aalbers et al. 2022). Additionally, the drift times of the two scatters are identical. This is not seen directly in the double scatter data as the first S1 is missed in each case, but can be observed through the LZ event viewer as in Figure 3.5.

Because the two scatters in each pileup event are roughly co-spatial, these events are likely the result of stationary particles interacting with the liquid xenon twice in quick succession. In order to explain these pileup events, we theorize that there exists a small amount of an unknown radioactive isotope in the metal of the cathode. This long half-life material decays into a daughter isotope with a very short half-life which decays after a brief period. We believe this to be the most likely origin for such an overdensity of pileup events.

Although this theory is reasonable, the data does not fully support it. The pileup

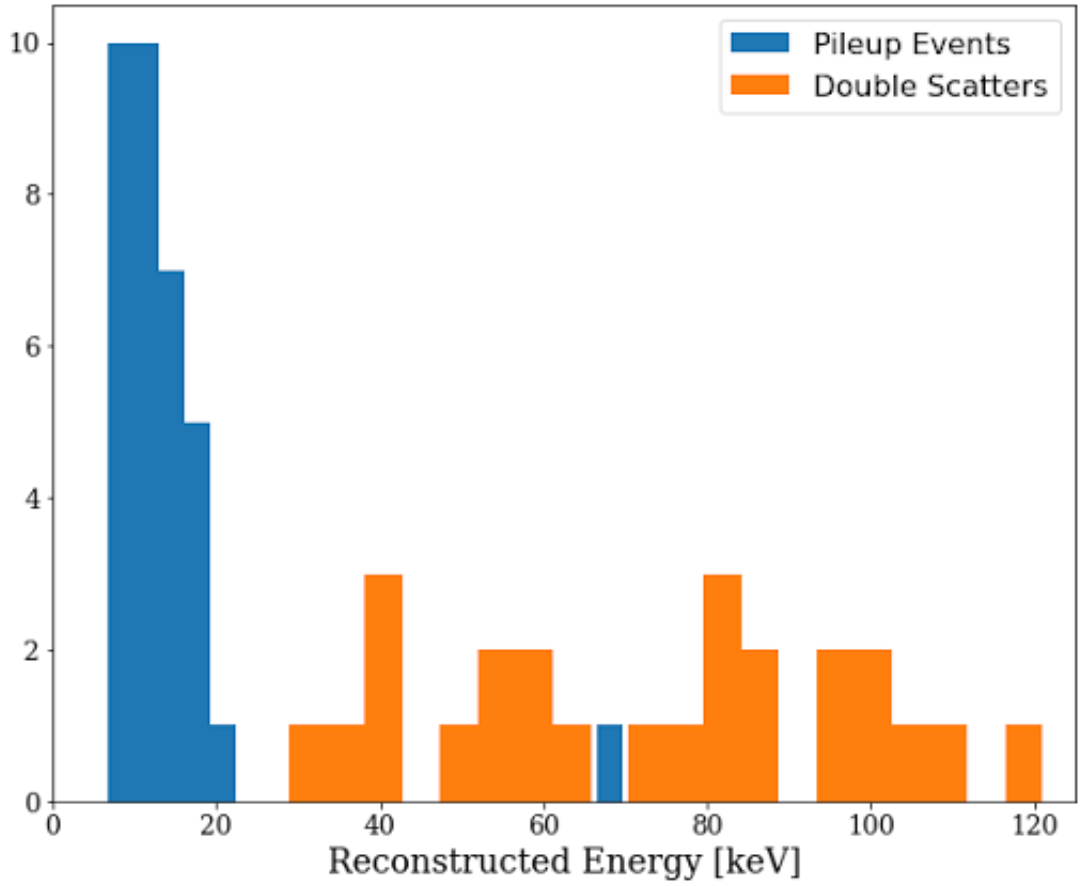

FIGURE 3.4: Overlaid histograms comparing the reconstructed event energy for pileup events and real events. Apart from a single outlier, the pileup events have significantly lower energy and a narrower energy distribution.

events we measure have an average time separation on the order of 100 μs. However, this does not fit with the decay of any known contaminants in the cathode. Additionally, radioactive decay rate over time is traditionally expected to follow a simple exponential decay function. In practice, the decay rate of the pileup events appears to fill a bimodal distribution in Figure 3.6. In order to come to an accurate conclusion on the origin of the pileup events, it will be necessary to look at more than the events that were mistaken for double scatters. By analyzing the pileup events originating from the cathode in a more detailed study, we would learn more about the LZ detector and potentially open up new avenues for reducing detector noise.

With the research we currently have, it appears that the cathode based pileup events are not a source of noise in the NR region. The pileup events occur outside

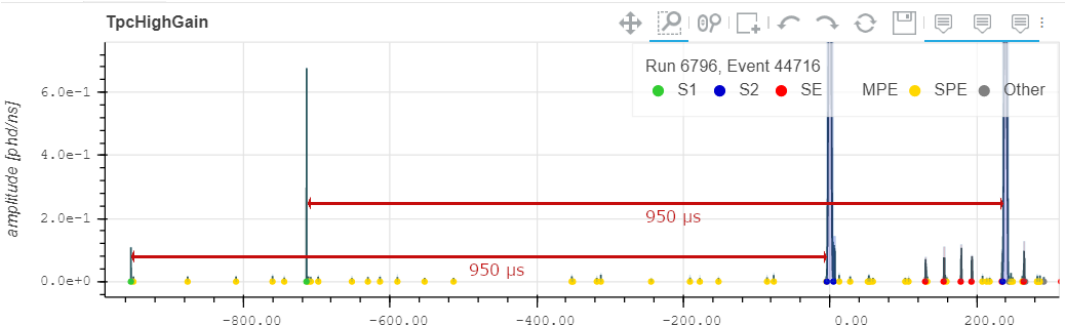

FIGURE 3.5: The waveform of a characteristic pileup event. The S1 at the far left was small enough that this event was mis-classified as a double scatter. The drift time for each scatter is shown with the red arrow marking the time between the S1 and S2 detections.

the FV and are only measured as being inside it because the S1 signals have a time separation. Conversely, an MSSI could only occur if the S1 signals had virtually zero time separation. Thus, all cathode-based pileup events that could be measured as MSSI will be removed by the FV cut and are not relevant to the NR background.

3.3 MSSI Leakage Rate

Using the simulated data and WIMP-nucleon bands we created, we calculated the MSSI leakage for each interaction model. The total number of leakage events for each operator is displayed in Table 3.1.

Of the 2 xenon-based MSSI expected during the first observing run of the LZ detector, the number that we expect to fall within the NR band ranges between 0.0144 and 0.0403 events. The spin independent model has the greatest leakage rate, with the spin dependent operators having slightly lower leakage. Apart from the difference between the spin dependent and spin-independent models, there is no significant pattern in leakage rates based on operator or WIMP mass.

Due to the low rate, the most likely case is that there is zero NR background due to xenon-based MSSI. However, the rate is high enough that we must include MSSI background in our calculations for the WIMP search. This will be especially

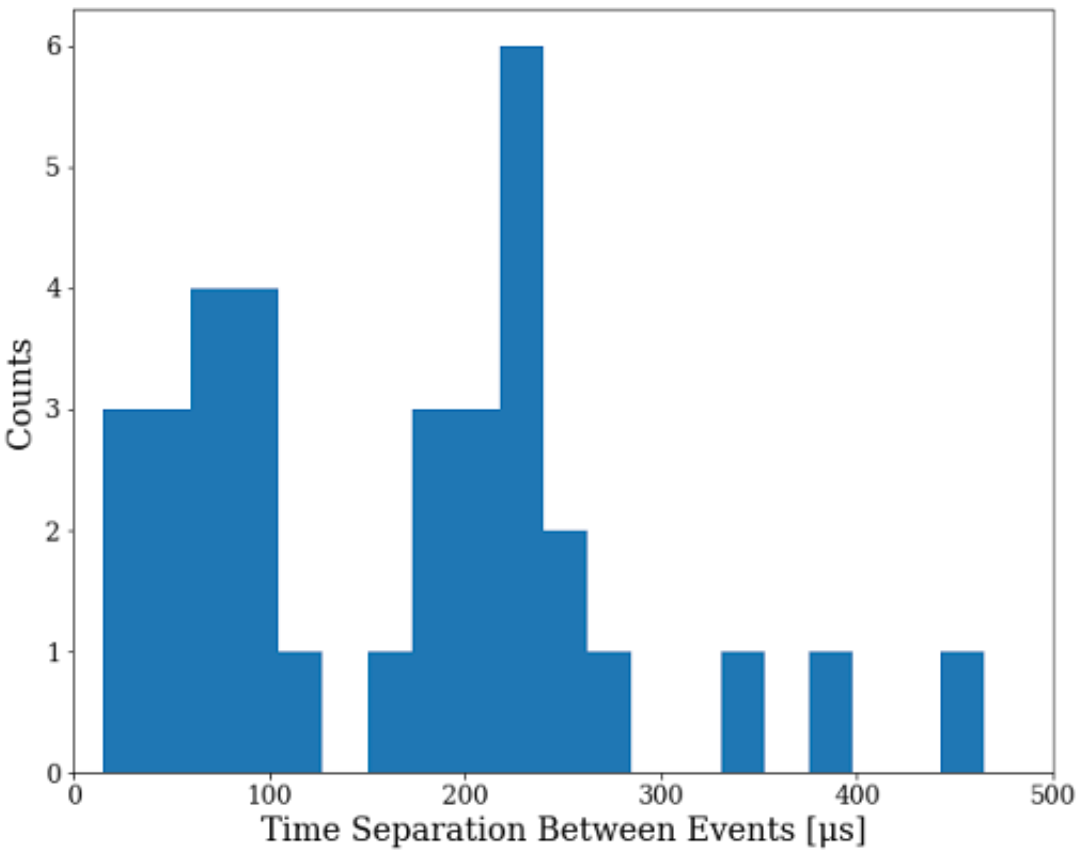

FIGURE 3.6: Histogram of the time separation between pileup events. If these were caused by two radioactive decays, we would expect the time separation to follow $A = A_0 e^{-\lambda t}$.

important as we observe for longer periods of time and the expected MSSI leakage rises.

3.4 ER Leakage Rate

Finally, we calculated the leakage rate of ER events into the NR band. The leakage rate below the NR 90% confidence level and band median as a function of S1 area is shown for the measured operators in Figures 3.7, 3.8, 3.9, 3.10, and 3.11.

Using the plots above, we can see a few commonalities in the leakage rates. The leakage rate peaks at the low end of S1 area, generally around 30 phd. Past 50 phd, the leakage rate drops quickly and falls to virtually zero by 200 phd. The

Interaction Model	Leakage [Events]
Operator 01 Default Uncertainty	0.0230 ± 0.015
Operator 01 Positive Uncertainty	0.0403 ± 0.025
Operator 01 Negative Uncertainty	0.0173 ± 0.01
Operator 03 400 GeV	0.0144 ± 0.01
Operator 03 4000 GeV	0.0173 ± 0.01
Operator 06 400 GeV	0.0154 ± 0.01
Operator 10 400 GeV	0.0182 ± 0.01
Operator 10 4000 GeV	0.0154 ± 0.01
Operator 13 400 GeV	0.0154 ± 0.01
Operator 13 4000 GeV	0.0163 ± 0.01

TABLE 3.1: Xenon-based MSSI leakage into NR band for a variety of interaction models. Leakage shown is expected number of events in the first observing run of LZ. The high uncertainty is primarily the result of the large estimated systematic uncertainties in the calculation for the total xenon-based MSSI.

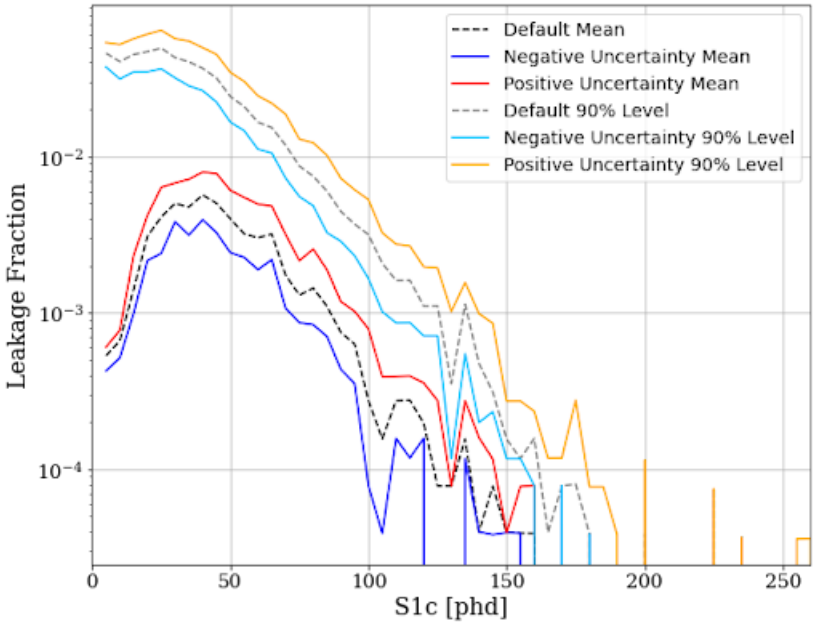

FIGURE 3.7: ER band leakage rate as a function of S1 area. Plotted are the leakages below the band median and 90% confidence level for the default flat NR band (Operator 01) as well as positive and negative uncertainties in the band.

peak leakage is roughly 0.05 below the 90% confidence level and ranges between 0.005 and 0.01 below the band mean for all interaction models.

Over the course of the first observing run of the LZ detector, we expect roughly

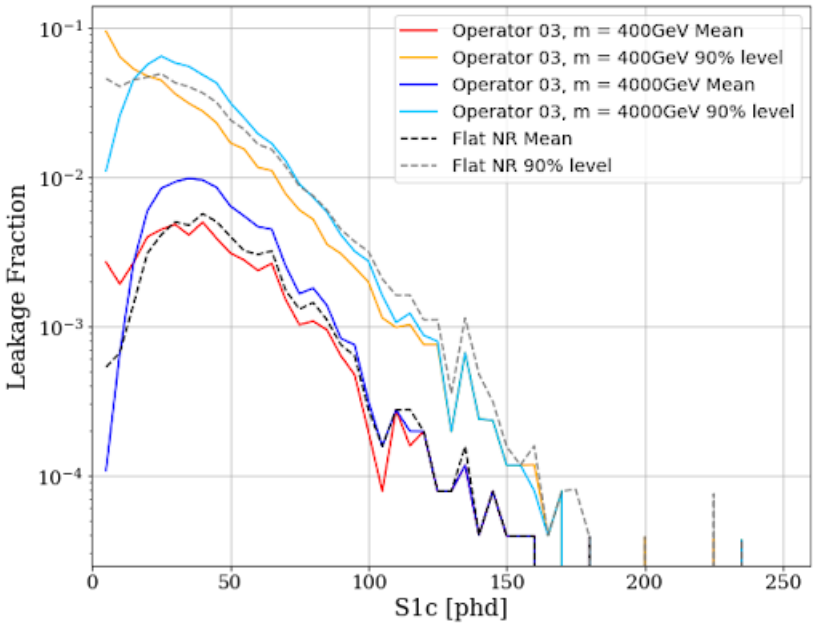

FIGURE 3.8: ER band leakage rate as a function of S1 area. Plotted are the leakages below the band median and 90% confidence level for Operator 03 with WIMP masses of 400GeV and 4000GeV. The leakage below the default flat band is displayed for comparison.

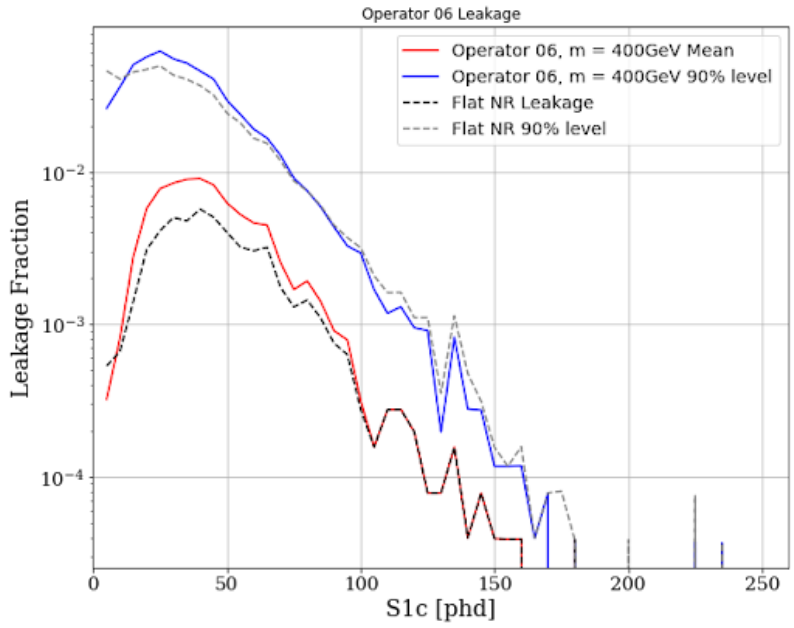

FIGURE 3.9: ER band leakage rate as a function of S1 area. Plotted are the leakages below the band median and 90% confidence level for Operator 06 with WIMP mass of 400GeV. The leakage below the default flat band is displayed for comparison.

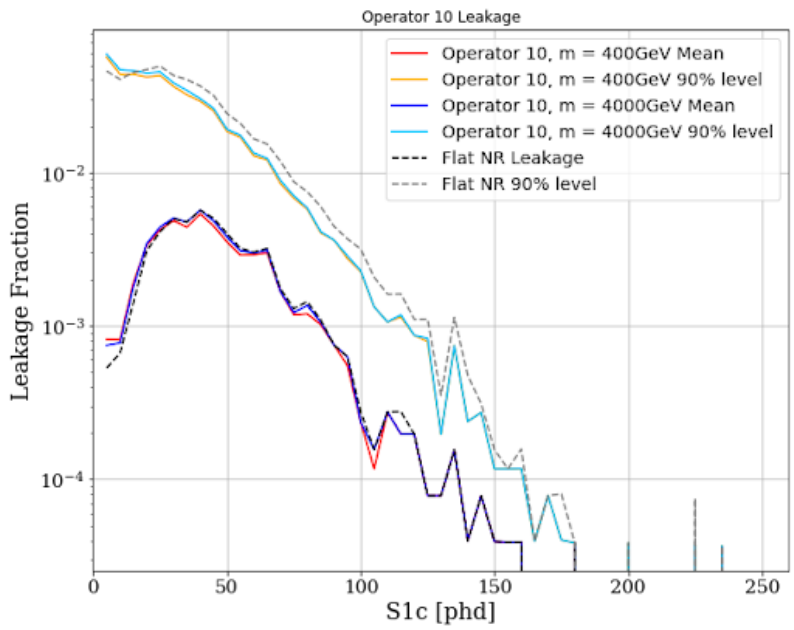

FIGURE 3.10: ER band leakage rate as a function of S1 area. Plotted are the leakages below the band median and 90% confidence level for Operator 10 with WIMP masses of 400GeV and 4000GeV. The leakage below the default flat band is displayed for comparison.

500 ER events below 200 phd. This number was calculated by extending the 200 events identified below 80 phd in Aalbers et al. (2022) and the flat ER spectrum at low energies. Using the leakage rates, we can approximate a few tens of ER events to leak into or below the NR band. This means ER leakage is by far the largest overall contributor to the NR background, with several orders of magnitude more events than either source of MSSI leakage. However, this leakage only occurs for low energy interactions. At higher energies, the ER and NR bands have diverged significantly and the leakage rate approaches zero. Thus, we expect a noisy background at low energies with just a few scattered background events at higher energies.

To accurately identify whether the data shows evidence of WIMP-nucleon interactions, the WIMP search will need to use not just the expected number of ER leakage events, but also their distribution. By comparing the distribution of events in the ER band to those in the NR band, researchers will be able to determine the statistical likelihood that the NR events emerged exclusively from ER leakage using the leakage rates we calculated. Although there is currently no way

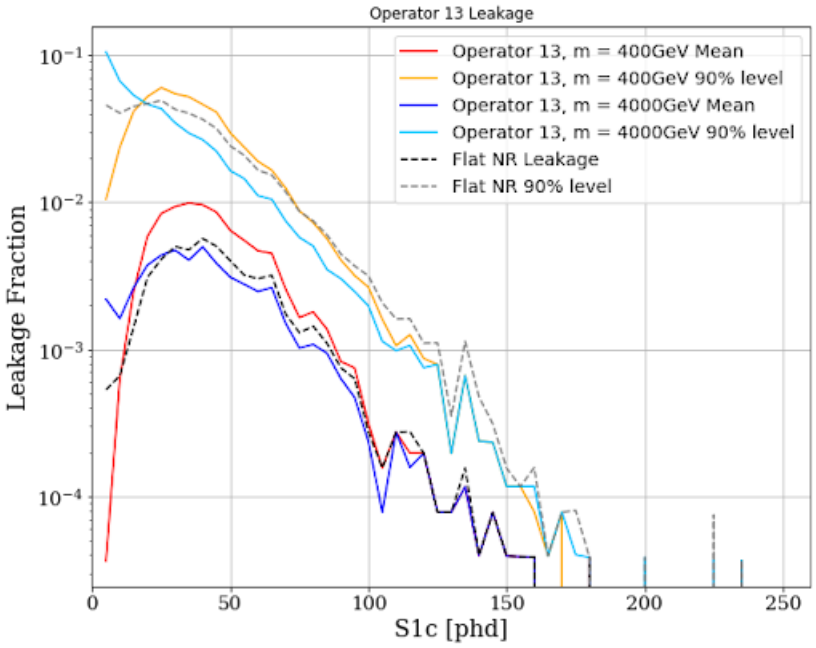

FIGURE 3.11: ER band leakage rate as a function of S1 area. Plotted are the leakages below the band median and 90% confidence level for Operator 13 with WIMP masses of 400GeV and 4000GeV. The leakage below the default flat band is displayed for comparison.

to completely eliminate the ER leakage contribution to the NR background, the leakage rate calculations allow us to search for WIMP-nucleon interactions that were previously hidden by the noise.

CHAPTER 4: Conclusion

By analyzing a combination of collected and simulated data, we have constructed a model of the expected NR background for a greater energy range than was used in Aalbers et al. (2022). The analysis shows that the vast majority of the contribution to the NR background results from ER leakage at low energies, which is in line with our predictions. The xenon-based MSSI have a small chance of falling within the NR band below 600 phd, and primarily occur at higher energies. Component-based MSSI have a near zero chance of originating from the cathode. The wall-based MSSI rate is likely low, but cannot be calculated accurately without an improved electric field model.

During Near Miss MSSI analysis, we identified a source of pileup events at the cathode. These events had a characteristic energy and event separation, so we concluded that they are likely the result of consecutive radioactive decays. Although we do not know the exact source or rate of these events, they do not contribute to the NR background.

The NR background that we have calculated will be used for statistical analysis in the WIMP search. The expected background based on detector time and ER event distribution will be compared to the data collected of events falling in the NR band. The greater range of our background model will allow the WIMP search to be sensitive to WIMP-nucleon interactions that occur at higher energies, such as through spin-dependent interaction models.

In the future, the most important extension to this work is likely to improve the electric field model at the edges of the detector. This will involve performing another calibration, as the detector environment from which we calibrated the previous model seems to have changed. Additionally, we would like to fix the issues with simulating WIMP-nucleon interactions for operators 06 and 15. The detailed leakage models created from this data could be important to determining the presence of DM in the data set, depending on the interaction type. Finally, we would like to do further research on the source of the pileup events we identified. The pileup events do not appear to interfere with the WIMP search, so this is

a lower priority. However, understanding these events is integral to constructing a more accurate model of the detector, and this understanding could potentially provide insight into an aspect of the WIMP search.

APPENDIX A: Fiducial Volume Cut Analysis

By definition, double scatters include two separate interactions, often taking place in different locations. Because of this, it is possible for one of the scatters to be in the FV and one to be outside it. In order to select an implementation for the cut, we compared three options. FV cut 1 required that both S2 pulses originated within the fiducial volume. FV cut 2 required that at least one of the scatters occurred in the FV. FV cut 3 similarly required that just one scatter occurred in the FV, but allowed the other scatter to fail the S2 quality cut and still be included in further calculations.

In order to select the appropriate FV cut, we ran our data through each cut combined with the rest of the standard cuts. By analyzing the resulting data structure, we identified the cut that best fit the data we were attempting to study. Although cut 1 most accurately eliminated false detections created by random noise, it also excluded much of the data most relevant to our study. MSSI events are characterized as double scatters in which one scatter is so close to the detector wall that its electrons are not detected. Thus, by excluding events with one xenon interaction close to the wall, we would be ignoring the events most similar to MSSI. In contrast to cut 1, FV cut 3 resulted in far too many false detections, especially at the low end of S1 area. The scatters that do not pass the quality cuts are highly unlikely to be real, resulting in a large number of single scatters with phantom second scatters remaining in the data. As single scatters cannot be MSSI, we concluded that FV cut 2 is the best cut to use for a Near Miss MSSI Search.

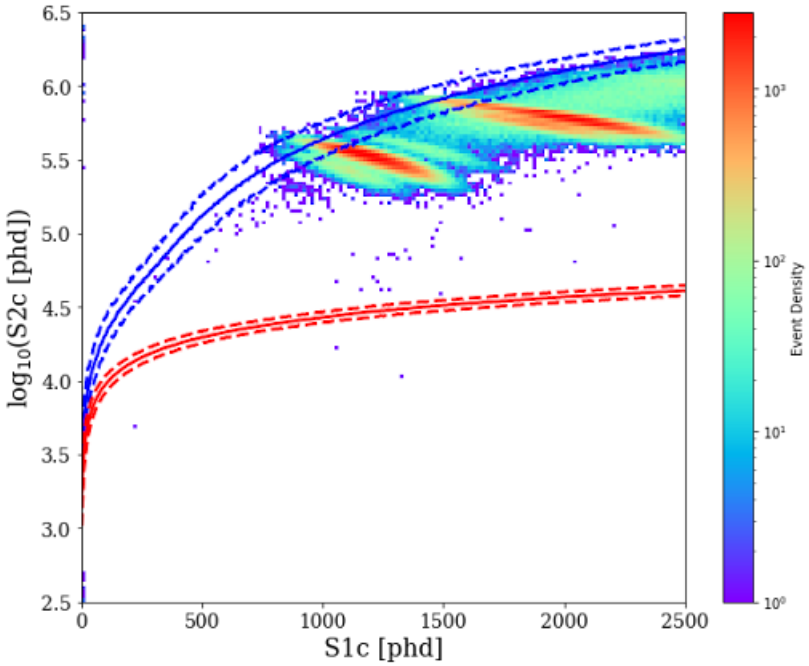

FIGURE A.1: Plot of double scatters that have passed all standard data cuts, including FV cut 1. This series of cuts has eliminated much of the random noise in addition to significant amounts of low energy ER events which we would like to study.

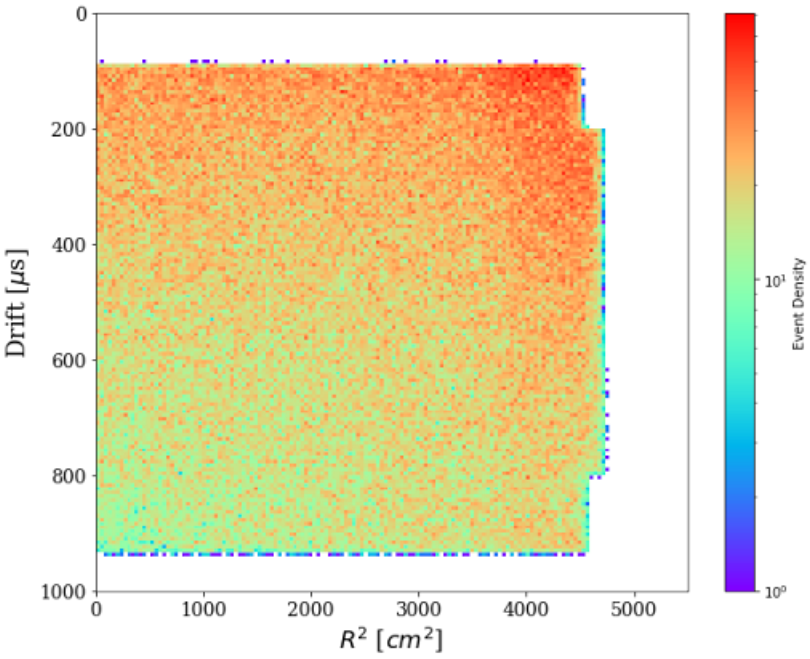

FIGURE A.2: Plot of the positions of double scatters that have passed all standard data cuts, including FV cut 1. There are no events outside the FV, though such events are similar to MSSI.

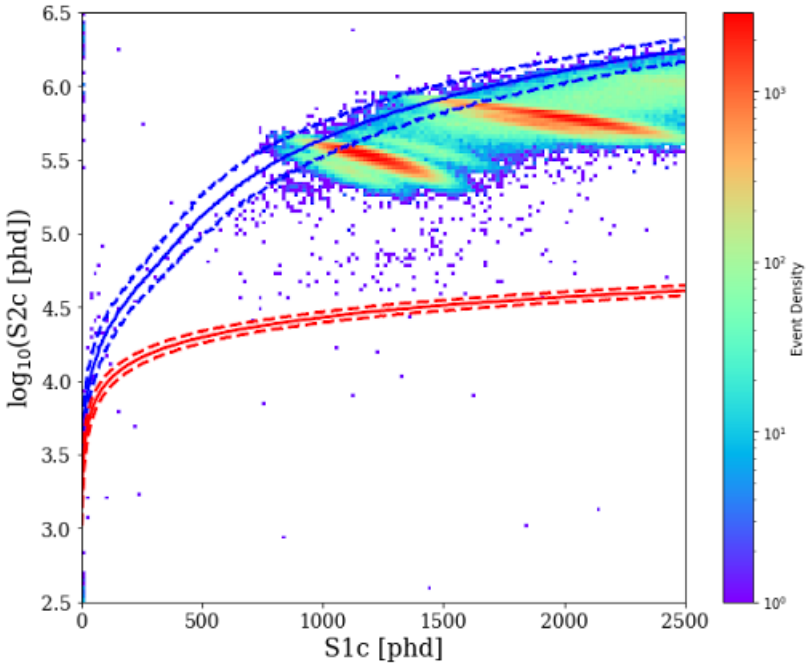

FIGURE A.3: Plot of double scatters that have passed all standard data cuts, including FV cut 2. This series of cuts has eliminated much of the random noise but leaves many of the low energy ER events which we would like to study.

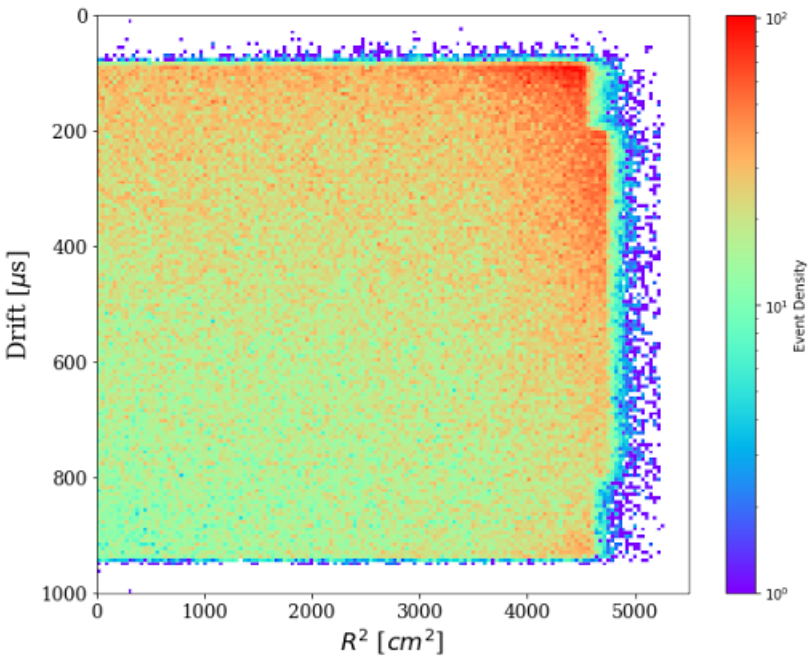

FIGURE A.4: Plot of the positions of double scatters that have passed all standard data cuts, including FV cut 2. There are some events outside the FV, though many are excluded.

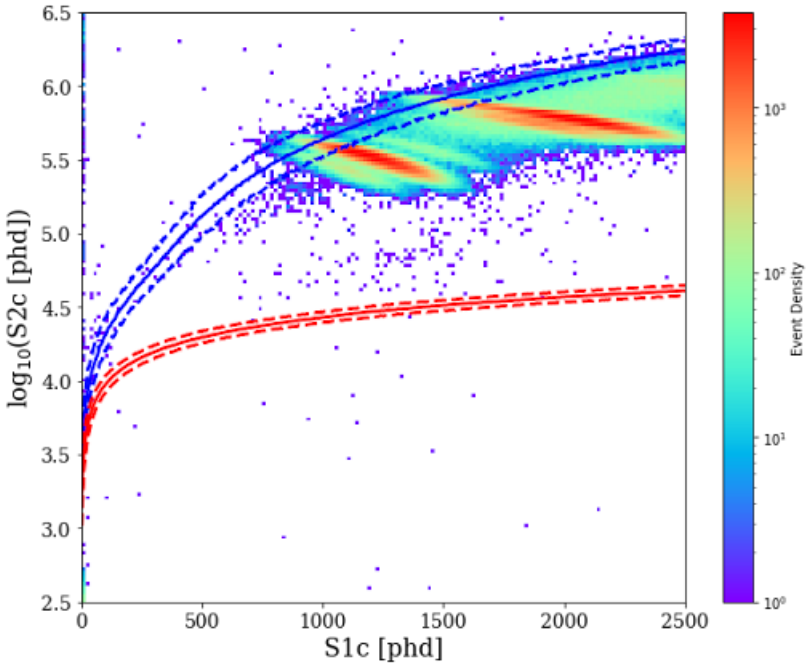

FIGURE A.5: Plot of double scatters that have passed all standard data cuts, including FV cut 3. This data is still very noisy, as events significantly above the ER band or below the NR band are unlikely to be real.

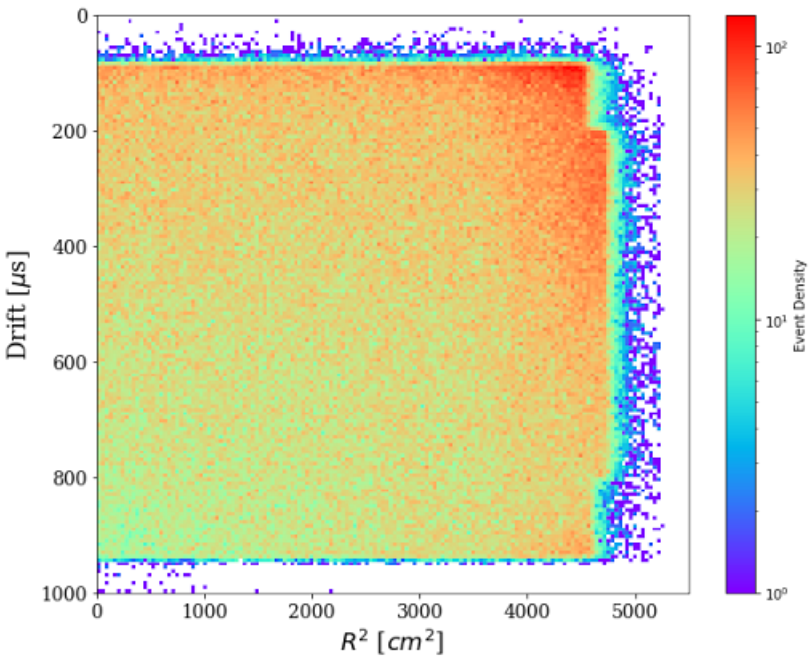

FIGURE A.6: Plot of the positions of double scatters that have passed all standard data cuts, including FV cut 3. There are many events outside the FV, including those that may not have a real scatter in the FV.

APPENDIX B: WIMP-Nucleon Recoil Bands

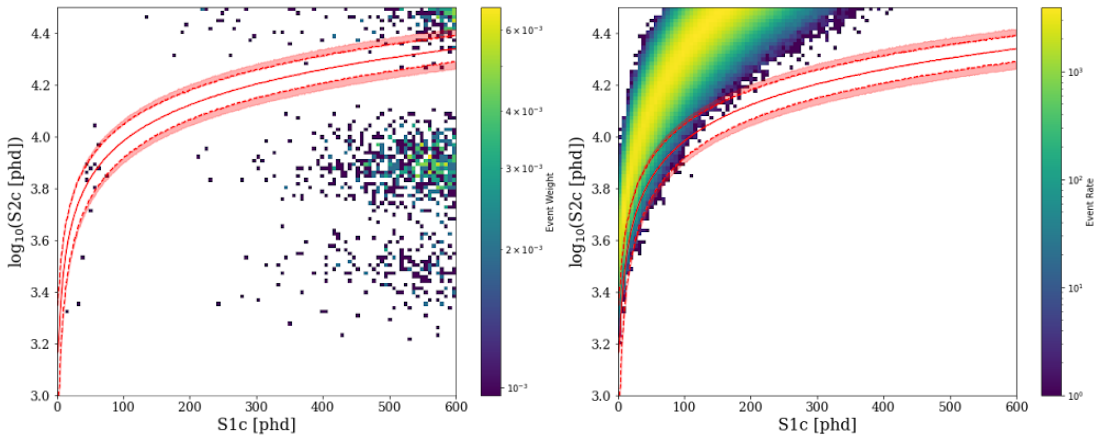

(A) MSSI Events (B) ER Events

FIGURE B.1: The flat NR band expected for spin independent WIMP-nucleon interactions plotted against simulated MSSI and ER events. The events that fall within the NR band form the NR background. The fringes for the positive uncertainty in the flat NR band is shown above the top dotted line and the negative uncertainty is shown below the bottom line.

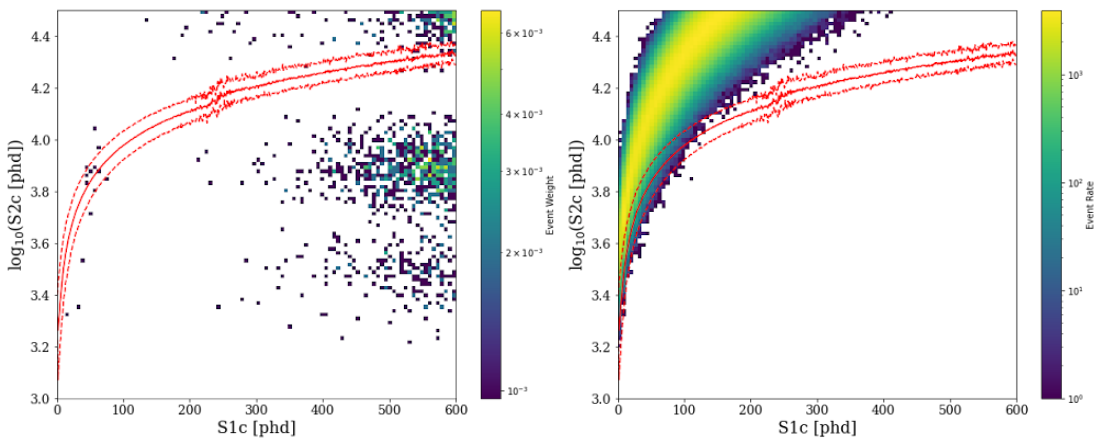

(A) MSSI Events (B) ER Events

FIGURE B.2: The NR band expected for nucleon interactions by 400GeV mass WIMPS through operator 03, plotted against simulated MSSI and ER events. The events that fall within the NR band form the NR background.

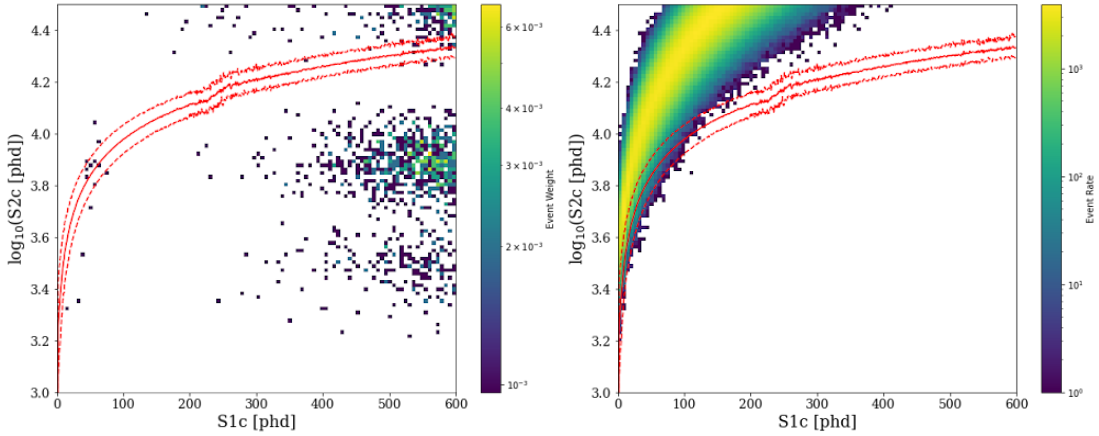

(A) MSSI Events (B) ER Events

FIGURE B.3: The NR band expected for nucleon interactions by 4000GeV mass WIMPS through operator 03, plotted against simulated MSSI and ER events. The events that fall within the NR band form the NR background.

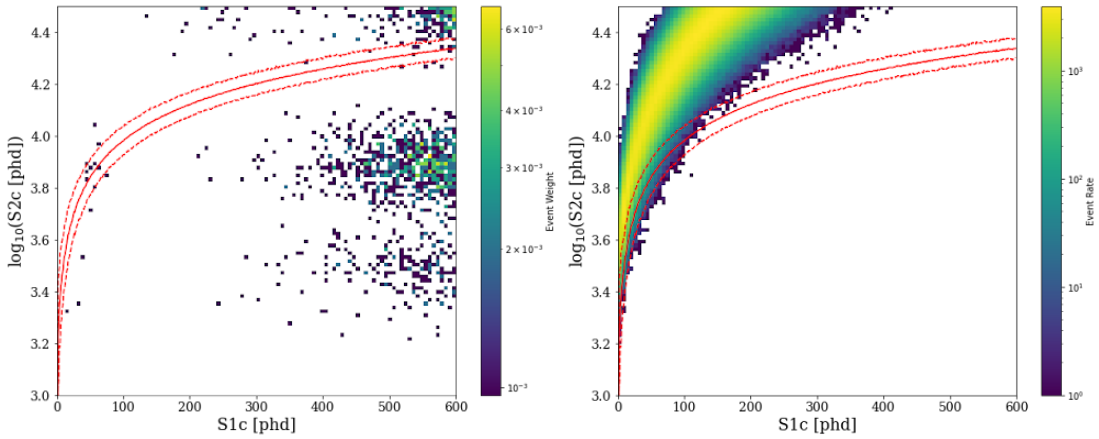

(A) MSSI Events (B) ER Events

FIGURE B.4: The NR band expected for nucleon interactions by 400GeV mass WIMPS through operator 06, plotted against simulated MSSI and ER events. The events that fall within the NR band form the NR background.

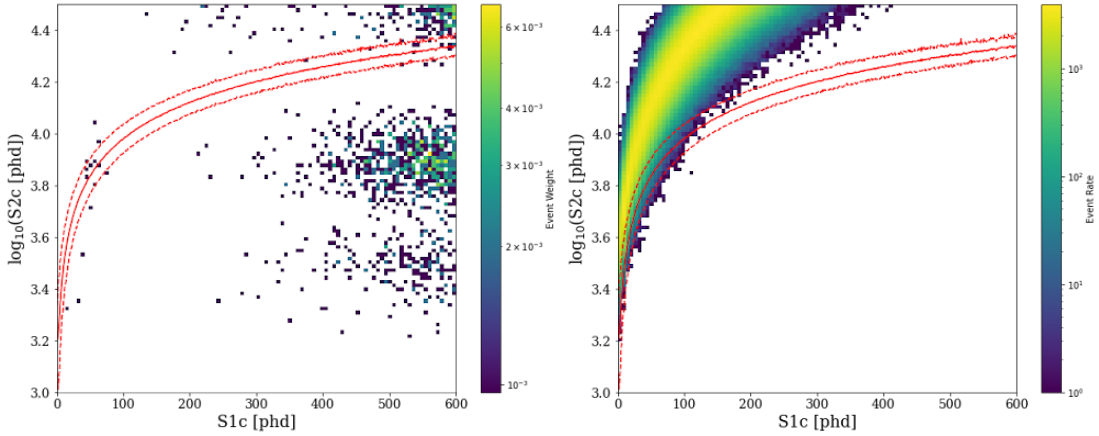

(A) MSSI Events (B) ER Events

FIGURE B.5: The NR band expected for nucleon interactions by 400GeV mass WIMPS through operator 10, plotted against simulated MSSI and ER events. The events that fall within the NR band form the NR background.

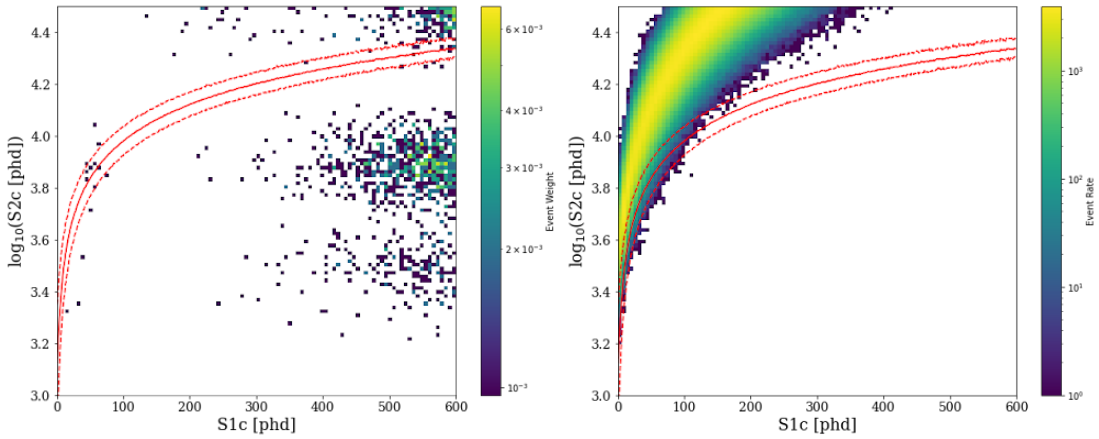

(A) MSSI Events (B) ER Events

FIGURE B.6: The NR band expected for nucleon interactions by 4000GeV mass WIMPS through operator 10, plotted against simulated MSSI and ER events. The events that fall within the NR band form the NR background.

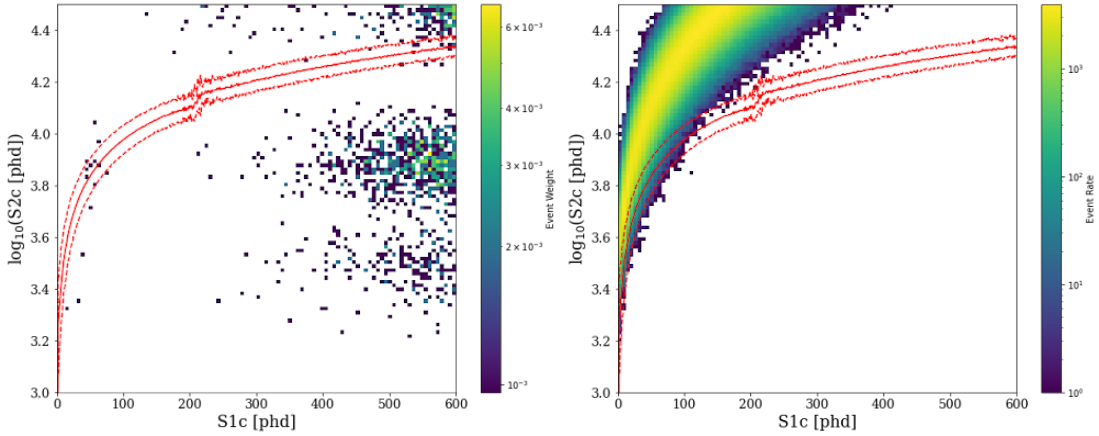

(A) MSSI Events (B) ER Events

FIGURE B.7: The NR band expected for nucleon interactions by 400GeV mass WIMPS through operator 13, plotted against simulated MSSI and ER events. The events that fall within the NR band form the NR background.

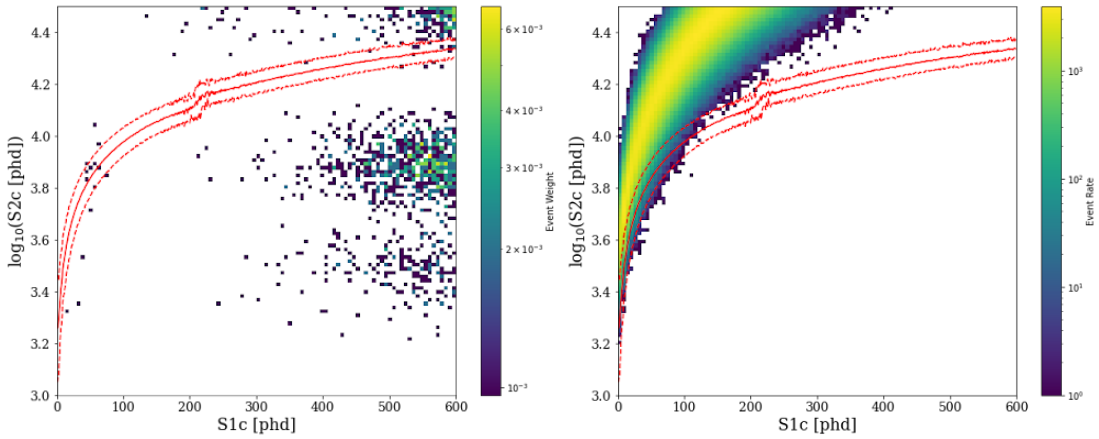

(A) MSSI Events (B) ER Events

FIGURE B.8: The NR band expected for nucleon interactions by 4000GeV mass WIMPS through operator 13, plotted against simulated MSSI and ER events. The events that fall within the NR band form the NR background.

APPENDIX B: Bibliography

Aalbers, J., Akerib, D. S., Akerlof, C. W., et al. 2022, arXiv e-prints, arXiv:2207.03764, doi: 10.48550/arXiv.2207.03764

Abe, T., Afik, Y., Albert, A., et al. 2020, Physics of the Dark Universe, 27, 100351, doi: 10.1016/j.dark.2019.100351

Akerib, D., Alsum, S., Araújo, H., et al. 2020, Physical Review D, 102, 112002

Andernach, H., & Zwicky, F. 1933, arXiv e-prints, arXiv:1711.01693, doi: 10.48550/arXiv.1711.01693

Baum, S., Catena, R., Conrad, J., Freese, K., & Krauss, M. B. 2018, Phys. Rev. D, 97, 083002, doi: 10.1103/PhysRevD.97.083002

Bertone, G., & Merritt, D. 2005, Modern Physics Letters A, 20, 1021, doi: 10.1142/S0217732305017391

Goodman, M. W., & Witten, E. 1985, Phys. Rev. D, 31, 3059, doi: 10.1103/PhysRevD.31.3059

Mount, B. J., Hans, S., Rosero, R., et al. 2017, arXiv e-prints, arXiv:1703.09144, doi: 10.48550/arXiv.1703.09144

Mullat, J. E. 2016, Journal of Cosmology, 26, 14992

Rischbieter, G. R. 2022, Signal Yields and Detector Modeling in Xenon Time Projection Chambers, and Results of an Effective Field Theory Dark Matter Search Using LUX Data (State University of New York at Albany)

Roszkowski, L., Maria Sessolo, E., & Trojanowski, S. 2018, Rep. Prog. Phys., 81, 2, doi: 10.1088/1361-6633/aab913

Szydagis, M., Barry, N., Kazkaz, K., et al. 2013, NEST: Noble Element Simulation Technique, Astrophysics Source Code Library, record ascl:1307.017. http://ascl.net/1307.017

Williams, M. 2022, in APS Meeting Abstracts, Vol. 2022, APS April Meeting Abstracts, B11.005